UNIVERSITY OF GENOVA

PHD PROGRAM IN BIOENGINEERING AND ROBOTICS

On the Volume Conduction Model Validation with Stereo EEG Data

by

Maria Carla Piastra

Thesis submitted for the degree of *Doctor of Philosophy* (33° cycle)

May 2019

Prof. Marco M. Fato — Supervisor

Prof. Giorgio Cannata — Head of the PhD program

Dibris

Department of Informatics, Bioengineering, Robotics and Systems Engineering

Declaration

I hereby declare that except where specific reference is made to the work of others, the contents of this dissertation are original and have not been submitted in whole or in part for consideration for any other degree or qualification in this, or any other university. This dissertation is my own work and contains nothing which is the outcome of work done in collaboration with others, except as specified in the text and Acknowledgements. This dissertation contains fewer than 65,000 words including appendices, bibliography, footnotes, tables and equations and has fewer than 150 figures.

Maria Carla Piastra
May 2019

Abstract

Volume conduction can be defined as the transmission of electric potential and magnetic field generated by a primary current source of brain activation in the surrounding medium, i.e., the human head.

Volume conduction simulations are based on sophisticated models whose construction represents a current challenge within the neuroscientific community.

Volume conduction models are used in various applications such as electroencephalography (EEG) or magnetoencephalography (MEG) source reconstruction, or in the optimization of the electrode placement in a transcranial electrical stimulation session. Clinical applications based on volume conduction models are, for example, the localization of the epileptogenic zone, i.e., the brain area responsible for the generation of seizures, in the presurgical assessment of focal drug-resistant epilepsy patients, and the antidepressant effects given by transcranial electrical stimulation. Increasing the accuracy of volume conduction simulations is therefore crucial.

To the best of our knowledge, the accuracy of volume conduction models have never been validated directly with actual measurements in human patients.

The main goal of this thesis is to describe a first attempt to validate volume conduction modeling using electric stimulation stereo-encephalografic (sEEG) data.

This work therefore is focused on the research, investigation and test of tools and methods which can be used to describe the accuracy of volume conduction models used in both clinical and basic research.

Given a dataset of one pharmaco-resistant epilepsy patient, composed by the anatomical T1 weighted magnetic resonance image (MRI), the electrophysiological signal recorded during electric brain stimulation sessions with sEEG technique and sEEG contact positions extracted by post-implantation CT image, the analysis conducted in this work can be split into three main steps.

First, we built volume conduction head models and we simulated the electric potentials during the electric brain stimulations. In this step, we solved the so-called (s)EEG forward problem by means of the finite element method in its classical formulation, and we considered

three different conductivity profile to assign to the computational domain, individually extracted by the T1-w MRI. Moreover we computed the solution in meshes with two different resolution, i.e., 1 mm and 2 mm, with three different ways to model the source term, i.e., the partial integration approach, the subtraction approach and Venant's approach.

Second, we extracted the responses to the electric brain stimulations from the actual sEEG measurements. Particular emphasis in this step was given to the optimal referencing systems of sEEG electrodes.

Third, we compared the simulated and measured potentials for each of the three volume conduction head models, both in a single shaft and global comparison.

The comparison results in overall high relative differences, with only slight modulations given by the distance from the stimulation site, the underlying volume conduction head model used and the compartment where the dipolar source is located.

Simulation results show that the computation of sEEG forward problem solution is feasible with the same scheme adopted for scalp EEG in the *duneuro* software (http://duneuro.org/), and it is stable for different mesh resolutions and source models also for intracranial electrodes, i.e., for electrodes close to the source positions.

From this first validation attempt, we can conclude that the distance contact-source modulates the relative error between measured and simulated potential; for the contacts in the white matter compartment we observed the most accurate results, and the results relative to the three and four compartment results were more accurate than the ones relative to the five compartment results. While we achieved topographical errors within 10% for most of the shafts, the amplitude of simulated and measured potentials notably differs.

Table of contents

List of figures

List of tables

Introduction

Electrical stimulation mapping (ESM) is essential for epilepsy surgery planning. The aim of ESM is to provide clear demonstration of the functional significance of the cortex in the seizure onset zone to minimize neurological morbidity during cortical resection.

StereoElectroEncephaloGraphy (sEEG) monitoring is an increasingly used intracranial presurgical technique, and pharmaco-resistant epileptic patients are indeed often implanted with sEEG electrodes and epileptic spikes are simultaneously induced (via electric pulses) and measured by means of the same configuration of intracranial sensors.

Not only in the context of presurgical epilepsy diagnosis, volume conduction simulations such as EEG or magnetoencephalography (MEG) source reconstruction and the optimization of sensor configuration for transcranial brain stimulation, are tools increasingly considered in the clinical practice.

In particular, in order to compute the EEG source reconstruction, i.e., to solve a related ill-posed inverse problem, the EEG forward problem has to be solved. Since the accuracy of EEG inverse problem solution depends strongly on the forward solution, it is fundamental to increase the accuracy of the latter (Brette and Destexhe, 2012).

In the EEG case, the forward problem consists of the evaluation of the electric potential generated by a source located in the brain by solving an elliptic partial differential equation (PDE) of second order (Wolters et al., 2007). In general, the accuracy of volume conduction (VC) simulations relies on different factors, such as the accuracy of the geometrical representation of the volume conductor head model, the exactness of the conductivity distribution of the different tissues through which the fields are transmitted, etc. In simplified scenarios, such as multilayer sphere models with piecewise homogeneous conductivity, analytical solutions are available (Brette and Destexhe, 2012).

In more realistic scenarios, e.g., realistically shaped head models, numerical methods have to be adopted. There is a large variety of numerical methods that can be employed, among them are boundary element methods (Acar and Makeig, 2010; Mosher et al., 1999; Stenroos and Sarvas, 2012), finite volume methods (Cook and Koles, 2006), finite difference

methods (Montes-Restrepo et al., 2014; Vatta et al., 2009; Wendel et al., 2008) and finite element methods (FEMs) (Bertrand et al., 1991; Drechsler et al., 2009; Marin et al., 1998; Nüßing et al., 2016; Pursiainen et al., 2016; Schimpf et al., 2002). Numerical solutions are usually validated in sphere models, where the analytical solution exists, and applied to solve the EEG forward problem in more realistically shaped volume conduction models. In particular, special emphasis is given to the sensitivity of numerical solutions to geometrical errors, different source models or different methods adopted.

To the best of our knowledge, in none of this studies a ground truth was built and compared to numerical solutions.

Therefore, the bio-engineering aim of this thesis is to investigate, test and identify tools and methods able to perform a validation of VC simulations and to obtain a ground truth extracted by ESM procedure in sEEG data.

Our work is therefore focused on the methods, showing a first attempt in validating VC simulation results with particular emphasis to the sEEG forward problem, analyzing encountered challenges.

Chapter 1

General Backgrounds

In this chapter we will introduce, first, the clinical background is presented; second, the biological background, where the origin or neuroscience, together with the basic electrophysiological mechanism which can be detected by neuroimaging techniques are illustrated; third, the assumptions at the basis of the mathematical model adopted for solving the (s)EEG forward problems are recalled; fourth, a description and comparison of the technological advantages and limitations of scalp EEG and intracranial EEG is given.

1.1 Clinical Background

Epilepsy is one of the most common neurological diseases in the world, as declared by the World Health Organization (de la Salud. Programme for Neurological Diseases et al., 2005). As of 2017, epilepsy is an important public health problem representing 0.6% of the global burden of disease.

Epilepsy is a neurological disorder that is characterized by an enduring predisposition to generate epileptic seizures and the associated cognitive, psychological and social consequences (Fisher et al., 2014).

Until the middle of the 19th century, epilepsy was widely assumed to be a vascular disease, but in 1849 Robert Bentley Todd, who was influenced by Michael Faraday's contemporary work on electromagnetism, came up with a new explanation to epilepsy that is based on the electric theory (Reynolds and Trimble, 2009; Todd, 1849). Nowadays it is known that an epileptic seizure is a transient behavioral change that might be objective signs or subjective symptoms caused by abnormal excessive or synchronous neuronal activity in the brain (Devinsky et al., 2018). Seizure onset can be focal (when abnormal neuronal activity arises in one or more localized brain regions or hemisphere), generalized (when abnormal neuronal

activity begins in a widespread distribution over both hemispheres) or of unknown onset (if the available clinical and laboratory data cannot identify whether the onset is focal or generalized) (Devinsky et al., 2018), see Figure 1.1.

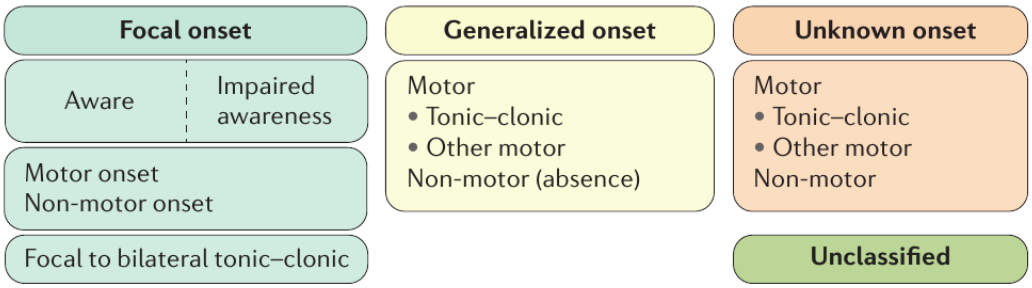

Figure 1.1 *Adapted from (Devinsky et al., 2018). According to the International League Against Epilepsy 2017 basic seizure classification, which is intended for use by practitioners not specializing in epilepsy, epileptic seizures can be classified as focal onset, generalized onset or unknown onset. When possible, focal seizures are divided into seizures with preserved awareness or with impaired awareness. Focal aware seizures were previously referred to as simple partial seizures, and focal impaired awareness seizures were previously referred to as complex partial seizures. Focal-onset, generalized-onset and unknown-onset seizures can include motor and non-motor forms. Focal seizures include seizures that progress to bilateral tonic–clonic seizures (formerly referred to as secondarily generalized tonic–clonic seizures). This classification also distinguishes between bilateral seizures (which propagate to both hemispheres) and generalized seizures (which originate simultaneously in both hemispheres).*

Onset is determined when there is >80% confidence about the mode of onset based on the clinical features, electroencephalography (EEG) and neuroimaging findings (Fisher et al., 2017), and the International League Against Epilepsy Classification framework, revised in 2017, is the key tool for the diagnosis of individuals presenting with seizures.

The first-line treatment for epilepsy is anti-seizure drugs (ASDs), of which > 20 drugs have been approved by the US FDA and the European Medicines Agency (Devinsky et al., 2018). However, despite the availability of many ASDs, approximately one-third of patients fail to achieve seizure control (Devinsky et al., 2018). Epilepsy surgery has the highest chance to render these patients seizure free, although only a small number of patients are eligible for surgery (Wiebe et al., 2001).

When surgery is not feasible on the patient (which is the case in the majority of the cases (Devinsky et al., 2018)) or when surgery fails in controlling seizures, neurostimulation devices, dietary therapies or clinical trials of new ASDs are alternative options.

In general, epilepsy is considered resolved when an individual is seizure free and older than the applicable age for an age-dependent epilepsy syndrome or, alternatively, when the

person has remained seizure free for ≥ 10 years with no anti-seizure medication for the past 5 years (Fisher et al., 2014).

There are many neuroimaging techniques which can help the identification of the epileptogenic zone, which is the area of the brain responsible for seizure generation: intracranial and scalp EEG, MEG, fNIRS, fMRI, etc.

In particular, interictal and ictal discharges can be observed and recorded at high temporal resolution using neurophysiology tools and electrodes that measure population events (the activity of multiple neurons) and single neuron activity, and are ideally studied by combining electrophysiology with functional or molecular imaging and optogenetics (Mantoan Ritter et al., 2014).

The diffusion of long-term (5–10 days) recording with intracranial and intracerebral electrodes during presurgical diagnostic monitoring in patients with drug-resistant focal epilepsy promoted research on human ictogenesis, which is the study of mechanisms generating seizures (Devinsky et al., 2018). This research focused on identifying biomarkers of the epileptogenic zone and ictogenesis (David et al., 2011; Gnatkovsky and Francione, 2014), studying cortical processing during cognitive tasks and cortical function, and epileptic network mapping (David et al., 2011).

The first epilepsy surgery was performed by William Macewen in 1879 and until the invention of EEG in 1929 by Hans Berger, the main source of information for the surgery was the seizure semiology observed by the physician (Berger, 1929; Kuzniecky and Jackson, 1995; Macewen, 1879). The seizure semiology, however, cannot be used as a reliable method in the diagnosis of epileptogenic brain areas that are away from the motor areas as in the case of temporal lobe epilepsy. Only after 1951, when 25 patients were operated based on the EEG, EEG has gained a wide acceptance as a powerful diagnostic method for the epilepsy surgery (Bailey and Gibbs, 1951; Kuzniecky and Jackson, 1995). In recent years, the number of epilepsy surgeries is increasing especially in the developed countries due to the advancements in pre-operative epilepsy evaluation.

1.2 Biological Background

Already in the XIX century the cells were assumed to be the fundamental unit of all living organs. The extremely complex organization of the nervous tissue, together with an inadequate technology, let the biologists of that period think that the nervous tissue rather had a net structure. The Italian biologist Camillo Golgi referred to that as *reticulum*. On the other side, by means of Golgi's staining method to visualize biological tissue (Golgi,

1873), the Spanish neuroanatomist Santiago Ramón y Cajal and the British physiologist Charles Sherrington replaced Golgi's reticular theory with the so called *neuron doctrine*. They claimed that nerve cells are discrete entities which communicate with one another by means of specialized contacts, i.e., synapses. The neuron doctrine was confirmed only in the 1950s with the advent of electron microscopy. Nevertheless, both Golgi and Cajal were awarded with the Nobel prize in 1906 in Physiology and Medicine for their findings on the organization of the nervous system and in 1932 also Sherrington was recognized for his contribution. The intense debate between especially Golgi and Cajal can be seen as the starting point of modern neuroscience.

The histological studies of Cajal, Golgi, and a host of successors led to the consensus that

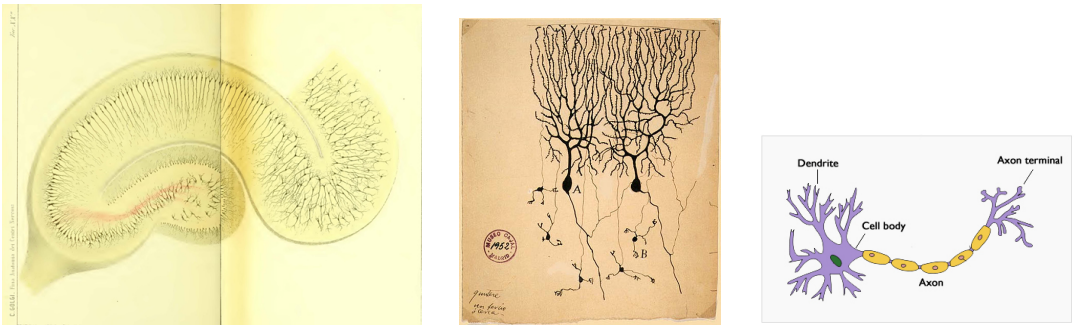

Figure 1.2 *Golgi's drawing of the hippocampus, based on tissues he had stained. From Golgi's 1886 publication "Sulla fina anatomia degli organi centrali del sistema nervoso." (on the left); 1899 drawing of Purkinje cells (A) and granule cells (B) from pigeon cerebellum by Santiago Ramón y Cajal. [image © Instituto Cajal, Madrid, Spain] (in the center); Schematic representation of the anatomy of the neuron (on the right).*

the cells of the nervous system can be divided into two broad categories: nerve cells, or neurons, and glial cells. The human brain is estimated to contain about 86 billion neurons and at least that many glial cells (Purves et al., 2018). While nerve cells are devoted to electrical signaling over long distances, glial cells are supporting nerve cells and do not generate a signal themselves. Each neuron consists of a cell body, dendrites, and an axon (see Figure 1.2, on the right). The cell body contains the nucleus and cytoplasm. The axon extends from the cell body and often gives rise to many smaller branches before ending at nerve terminals. Dendrites extend from the neuron cell body and receive messages from other neurons. Synapses are the contact points where one neuron communicates with another. The dendrites are covered with synapses formed by the ends of axons from other neurons. Neurons never function in isolation; they are organized into ensembles called neural circuits that process specific kinds of information and make up neural systems that serve broader

purposes. The most general functional distinction divides such collections into sensory systems, motor systems and associational systems (Purves et al., 2018).
A more detailed picture of the events underlying any neural circuit can be obtained by electrophysiological recording, which measures the electrical activity of nerve cells (Purves et al., 2018). With EEG the electric potential differences are measured by means of electrodes positioned on the scalp of the patient or healthy subject. This method was initially adopted in clinical practice to localize epileptic foci and epileptogenic cortical tissue for presurgical diagnosis. First attempts were made at the Montreal Neurological Institute by Herbert Jasper and Wilder Panfield. Due to the non-invasive nature of this technique, EEG was thereafter used for basic research on healthy subjects. Similarly to EEG, the MEG measures brain activity by recording magnetic fields produced by electrical currents generated in the brain. Neuromagnetic signals are typically between 50 and 500 fT, therefore the MEG method is based on the superconducting quantum interference device or SQUID, a sensitive detector of magnetic flux, introduced in the late 1960s by James Zimmerman (Hämäläinen et al., 1993; Zimmerman et al., 1970). The first SQUID measurement of magnetic fields of the brain was carried out at the Massachusetts Institute of Technology by David Cohen (Cohen, 1972). He measured the spontaneous α activity of a healthy subject and the abnormal brain activity of an epileptic patient (Hämäläinen et al., 1993). MEG is closely related to EEG. In both methods, the measured signals are generated by the same synchronized neuronal activity in the brain. The time resolution of MEG and EEG is in the millisecond range, orders of magnitude better than in almost any other techniques adopted in neuroscience (Hämäläinen et al., 1993). Both EEG and MEG are completely non-invasive techniques.

In general, nerve cells generate a variety of electrical signals that transmit and store information (Purves et al., 2018). Two main electrical signals are generated by neurons: action potentials and post-synaptic potentials. The action potential can be approximated with a current quadrupole, while a synaptic current flow with a dipole. The decay of an action potential is therefore faster ($1/r^3$, with r being the distance) than the one of a synaptic potential ($1/r^2$). Furthermore, temporal summation of currents flowing in neighboring fibers is more effective for synaptic currents, which last tens of milliseconds, than for action potentials, which have a duration of one millisecond only (Hämäläinen et al., 1993). Thus EEG and MEG signals are produced in large part by synaptic current flow, which is approximately dipolar (Hämäläinen et al., 1993; Murakami and Okada, 2006; Okada, 1993).

Finally, neuroscientists and neurologists have conventionally divided the vertebrate nervous system anatomically into central and peripheral components (Purves et al., 2018). The central nervous system (CNS) comprises the brain (cerebral hemispheres, diencephalon,

cerebellum, and brainstem) and the spinal cord. The peripheral nervous system (PNS) includes the sensory neurons that link sensory receptors on the body surface or deeper within it with relevant processing circuits in the CNS (Purves et al., 2018). Two gross histological terms distinguish regions rich in neuronal cell bodies versus regions rich in axons. Gray matter refers to any accumulation of cell bodies in the brain and spinal cord. White matter (named for its relatively light appearance, the result of the lipid content of myelin) refers to axon tracts and commissures (Purves et al., 2018). Within gray matter, nerve cells are arranged in two different ways. A local accumulation with neurons that have roughly similar connections and functions is called a *nucleus*; such collections are found throughout the cerebrum, diencephalon, brainstem, and spinal cord. In contrast, *cortex* describes sheetlike arrays of nerve cells. Within the white matter of the CNS, axons are gathered into tracts that are more or less analogous to nerves in the periphery (Purves et al., 2018).

1.3 Mathematical Background

In this section the mathematical model adopted to emulate the generation of electric potentials inside a human head, i.e., the EEG and forward problem, is deduced.

1.3.1 Derivation of the EEG Forward Problem

Following (Hämäläinen et al., 1993) and (Brette and Destexhe, 2012), the electric potential distribution and the resulting magnetic induction generated in the brain can be modeled through the quasi-static approximation of Maxwell's equations, when assuming that the permeability of the tissue in the head is that of the free space, i.e., $\mu = \mu_0$,

$$\nabla \times \mathbf{E} = 0, \tag{1.1a}$$
$$\nabla \cdot \mathbf{E} = \frac{\rho}{\varepsilon_0},$$

related to the electrical part, and

$$\nabla \times \mathbf{B} = \mu_0 \mathbf{j}, \tag{1.2a}$$
$$\nabla \cdot \mathbf{B} = 0, \tag{1.2b}$$

related to the magnetic part, where $\mathbf{E}$ is the electric field, $\mathbf{B}$ the magnetic field, ρ is the electric charge density, ε_0 is the permittivity of free space and μ_0 is the permeability of free

space. In (1.2a) $\mathbf{j}$ represents the total current density produced by neuronal activity, which, in bio-electromagnetism (Brette and Destexhe, 2012; Hämäläinen et al., 1993), is split into two contributions,

$$\mathbf{j}(\mathbf{r}) = \mathbf{j}^p(\mathbf{r}) + \mathbf{j}^s(\mathbf{r}), \tag{1.3}$$

where $\mathbf{j}^p$ is the so called primary current, $\mathbf{j}^s$ the secondary or volume current and $\mathbf{r} \in \mathbb{R}^3$. In neuromagnetism, the primary current is widely represented as a *mathematical point dipole* (De Munck et al., 1988; Murakami and Okada, 2006),

$$\mathbf{j}^p(\mathbf{r}) = \mathbf{M} \cdot \delta(\mathbf{r} - \mathbf{r}_0), \tag{1.4}$$

where $\mathbf{M} \in \mathbb{R}^3$ stands for the dipolar moment and δ is the Dirac delta distribution centered in the dipole position $\mathbf{r}_0 \in \mathbb{R}^3$.
The volume current is a passive current that is the result of the macroscopic electric field on charge carriers in the conducting medium (Brette and Destexhe, 2012; Hämäläinen et al., 1993), and

$$\mathbf{j}^s = \sigma\mathbf{E} \tag{1.5}$$

holds true (Ohm's law), where σ indicates the conductivity profile of the conductive medium. While for the mathematical point dipole the primary current is present only at the source position, the secondary current flows passively everywhere in the medium.

The Forward Problem of EEG

To derive the EEG forward problem, (1.1a) and (1.2a) have to be considered. As a consequence of (1.1a), there exists a potential u such that

$$\mathbf{E} = -\nabla u, \tag{1.6}$$

so that (1.5) can be written as

$$\mathbf{j}^s = -\sigma\nabla u. \tag{1.7}$$

Applying the divergence to (1.2a), we obtain

$$\nabla \cdot \mathbf{j} = 0. \tag{1.8}$$

Combining (1.3), (1.7) and (1.8), we get an inhomogeneous Poisson equation that, together with the homogeneous Neumann boundary condition, models the EEG forward problem:

$$\nabla \cdot (\sigma \nabla u) = \nabla \cdot \mathbf{j}^p (= f), \qquad \text{in } \Omega \subseteq \mathbb{R}^3 \tag{1.9}$$

$$\sigma \nabla u \cdot \mathbf{n} = 0, \qquad \text{on } \partial\Omega \tag{1.10}$$

where Ω is the volume conductor and $\mathbf{n}$ is the unit outer normal vector on $\partial\Omega$.
The EEG forward problem consists in finding the electric potential u on the domain Ω, assuming to know σ and $\mathbf{j}^p$. The strong formulation, as it appears in (1.9), admits a solution $u \in \mathscr{C}^2(\Omega)$ if restrictions are imposed on the source term f and the conductivity tensor σ. In this framework, the usual assumptions on this model are that, for example, the conductivity tensor is only piecewise constant, i.e., $\sigma \in L^\infty(\Omega)$ and that $\mathbf{j}^p$ is a distribution, see (1.4). The idea is then to relax the conditions required to the solution u by introducing the weak formulation of the problem, which reads: find $u \in V$ such that

$$\int_\Omega \sigma \nabla u \cdot \nabla v \, \mathrm{d}x = \int_\Omega f v \, \mathrm{d}x, \ \forall v \in V.$$

The weak formulation can be deduced by multiplying the strong formulation for a so-called test function $v \in V$, integrating the resulting equation in the domain Ω and using Gauss' theorem (in a heuristic way) to manipulate the left-hand side. The weak formulation can also be written in terms of both a linear and a bilinear operators, i.e., find $u \in V$

$$a(u,v) = l(v), \ \forall v \in V,$$

where

$$a(u,v) = \int_\Omega \sigma \nabla u \cdot \nabla v \, \mathrm{d}x,$$
$$l(v) = \int_\Omega f v \, \mathrm{d}x.$$

While in the strong formulation, the solution should be looked for in $V = \mathscr{C}^2(\Omega)$, for the weak formulation, it suffices that u belongs to the Sobolev function space $H^1(\Omega)$, or, more precisely, in the quotient $H^1_*(\Omega)$, following the definitions

$$H^1(\Omega) := \left\{ f \in L^2(\Omega) : D^1 f \in L^2(\Omega) \right\},$$

and

$$H^1_*(\Omega) := \left\{ f \in H^1(\Omega) : \int_\Omega f \, \mathrm{d}x = 0 \right\}.$$

When choosing $V = H^1_*(\Omega)$, it is possible to proof consistency with the strong formulation together with existence and uniqueness of the solution. More details can be found , e.g., in (Vorwerk, 2016).

1.3.2 A Conservation Property

A fundamental physical property of the EEG forward problem is the conservation of charge:

$$\int_{\partial K} \mathbf{j}^s \cdot \mathbf{n} \, \mathrm{d}s = \int_K f \, dK, \; \forall K \subset \Omega,$$

where $f = -\nabla \cdot \mathbf{j}^p$ and K is a control volume in Ω. For FEMs this property carries over to the discrete solution only if the test space contains the characteristic function, which is one in K and zero everywhere else. In general, a conforming discretization does not guarantee this property, while the discontinuous Galerkin finite element method fulfills a discrete analogue. More details will follow.

1.4 Technological Background

The first study involving intracranial electroencephalography (iEEG) was conducted by Berger in (Gloor, 1969), when he implanted needle electrodes and recorded brain activity. Thereafter, scientists as Förster, Altenburger and Delgado further developed the technique initiated by Berger in order to study tumors and psychic patients, respectively. In 1938 Panfield and Jasper were the first ones who utilized iEEG to investigate epilepsy. They indeed recorded brain activity from bilateral electrodes positioned on the dura in order to lateralize seizure onset (Almeida et al., 2005). Later on, in 1962, Banrad and Talairach introduced the stereoEEG technique to investigate brain activity in pharmacoresistant epileptic patients (Talairach et al., 1962).

Nowadays different iEEG recording techniques are worldwide utilized in many epilepsy centers. In particular, stereoEEG is traditionally adopted more in countries like France, Italy and Canada, while subdural grids, strips, or a mix with depth electrodes are mainly used in the US as iEEG tools (Kovac et al., 2017), see Figure 1.3.

The percentage of patients considered for epilepsy surgery in need for iEEG ranges approximately between 30% and 40% in tertiary epilepsy centers (Kovac et al., 2017). The

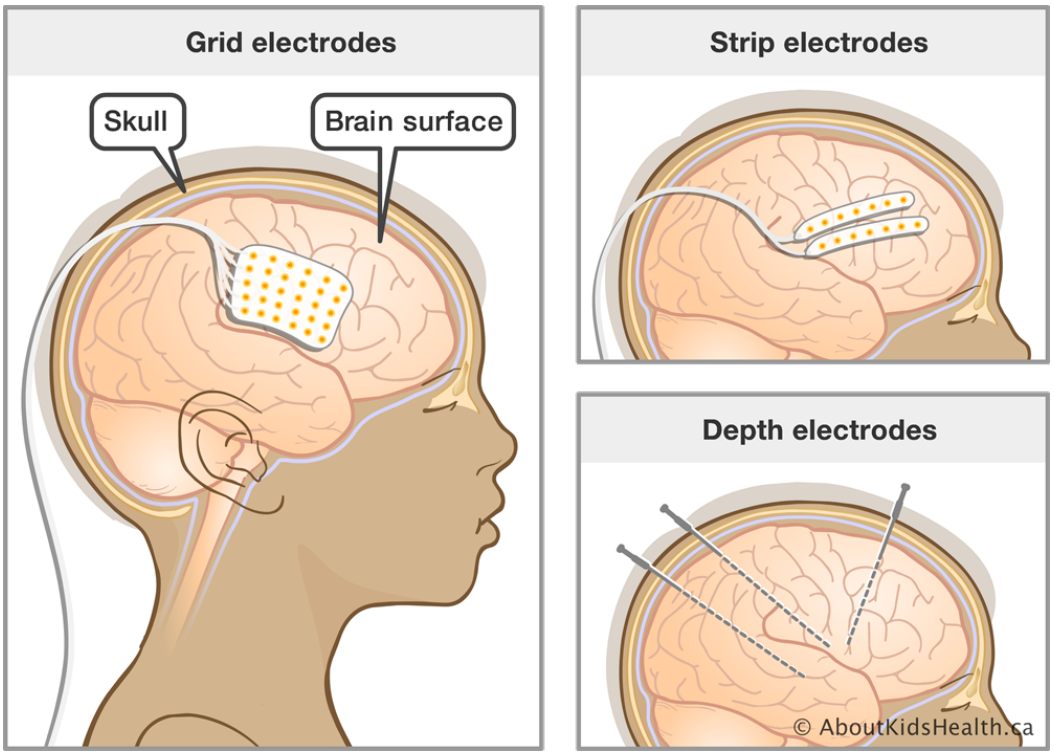

Figure 1.3 *Invasive grid and strip electrodes are placed on the surface of the brain. While depth electrodes are placed into the deeper parts of the brain. From www.aboutkidshealth.ca*

advancement and diversity of different iEEG techniques allows for the exploration of more complex epilepsies which requiring more extensive sampling and implantation of riskier structures such as insular cortex (Kovac et al., 2017).

IEEG helps to establish surgical candidacy and to delineate surgical margins. It is often needed to complement or resolve contradictory findings obtained by non-invasive tests (Kovac et al., 2017). Decision on surgical candidacy and whether iEEG recordings are needed is typically made in a multidisciplinary team meeting after patients have undergone a number of non-invasive investigations, such as, e.g., careful history and analysis of seizure semiology, scalp video EEG, neuropsychological and neuropsychiatric testing, structural and often also functional imaging such as PET and ictal SPECT. Advanced neurophysiological options include magnetoencephalography or high density EEG (Cardinale et al., 2012; Kovac et al., 2017).

The aim of iEEG recordings is dual. First, to aid defining the epileptogenic zone (EZ), which is defined as the minimum cortical area that needs to be removed to render the patient seizure free (Rosenow and Lüders, 2001). Second, to determine the location and extent of eloquent cortex in relation to the EZ to define safety margins for epilepsy surgery via direct

electrical cortical stimulation mapping (CSM) through the same electrodes, in order to add information about the cortex which needs to be spared during resection (Kovac et al., 2017).

IEEG has several advantages over scalp EEG for the identification of the EZ. For example, iEEG tools have higher spatial resolution and are able to detect a larger frequency range of brain signals when compared to scalp EEG. Moreover, despite scalp EEG, iEEG recordings do not suffer from muscle artifacts and the signals are not attenuated by the scalp and skull compartments.

In sEEG the strategy adopted to identify the EZ is based on the "anatomical-electrical-clinical correlation", as conceptualized by Bancaud and Talairach (Kovac et al., 2017). The method relies on interpreting a seizure network by looking at both semiology, intracranial sEEG recordings and, in some cases, seizures stimulated by CSM (Kahane et al., 2006; Kovac et al., 2016, 2017).

The planning of the implantation of sEEG electrodes involves multidisciplinary approach and multimodal neuroimaging techniques, such as, e.g., angiography, after implantation CT, pre and after MRI.

The main advantage of sEEG over subdural grid recording is that there is no need for a large craniotomy which adds to the morbidity (Kovac et al., 2017). The sEEG electrodes can be inserted via burr holes and do not require a second operation for removal of the electrode as is the case in subdural EEG (Kovac et al., 2017).

Despite subdural grids, with sEEG deep structures are accessible, reoperations requiring implantations are safer, and bilateral explorations are more doable (Kovac et al., 2017).

In general, when considering different iEEG techniques, it is currently not understood how various sampling strategies affect size of the resection and seizure and cognitive outcome (Kovac et al., 2017).

In (Mullin et al., 2016), where a meta-analysis summarizing 30 studies about the safety of sEEG has been conducted, they concluded that complications occurred with a pooled prevalence of 1.3%, much lower when compared to subdural EEG.

IEEG electrodes can both record cortical activity, but can also be used to stimulate the cortex underlying the electrode in subdural EEG recording or surrounding the electrode in depth electrode recording or sEEG (Kovac et al., 2017). In iEEG, CSM is used to map eloquent cortex (Kovac et al., 2011, 2014b). The advantage of extra-operative compared to intraoperative CSM is that there are less time constraints outside the operating theater. CSM is used to map language, motor and sensory function. Extra-operative CSM does not have the time limitations of intra-operative CSM. CSM is typically performed using up to 5 s trains of 50-Hz unipolar bi-phasic square wave pulses of an AC-current with a pulse width of 500 ms

(Kovac et al., 2014b). Either two adjacent electrodes are stimulated in bipolar stimulation mode or an electrode remote from eloquent cortex is referenced to an electrode overlying presumed eloquent cortex in so called 'monopolar stimulation mode' (Kovac et al., 2017).

In general, CSM can induce seizure with habitual or non-habitual semiology. Seizures with a non-habitual semiology are an unwanted side-effect of CSM (Kovac et al., 2014a). Habitual seizures induced via CSM, in contrast, have been used to define the epileptogenic network (Kovac et al., 2017).

Chapter 2

Volume Conduction Models and SEEG Data

In this chapter we describe how to create a volume conduction model and we present the sEEG dataset used in this thesis.

2.1 Volume Conduction Head Modeling

One of the key ingredients of the finite element method is a volumetric representation of the volume conduction (VC) head model.

In this study we constructed three different VC head models:

- a three compartment isotropic head model (3C), where the scalp, skin and brain compartments are identified;
- a four compartment isotropic head model (4C), where the cerebrospinal fluid (CSF) layer is added within the brain compartment of 3C;
- a five compartment isotropic head model (5C), where the brain compartment is further refined and the gray and white matter are discerned.

More details can be found in Table 2.1.

In this sub-chapter, the main steps necessary to build the three VC models are presented.

A T1-weighted magnetic resonance image (T1w MRI) of one epileptic patient was acquired.

The patient suffered from farmaco-resistant epilepsy and he is eligible for surgical intervention, following (Cardinale et al., 2012).

Tissue	5C (S/m)	4C (S/m)	3C (S/m)	
white matter	0.14	-	-	Ramon et al. (2004)
gray matter	0.33	-	-	Ramon et al. (2004)
brain	:	0.33	0.33	Ramon et al. (2004)
CSF	1.79	1.79	-	Baumann et al. (1997)
skull	:	0.01	0.01	Dannhauer et al. (2011)
skin	0.43	0.43	0.43	Dannhauer et al. (2011),Ramon et al. (2004)

Table 2.1 *Conductivity values (in S/m) of the three models created and used for the sensitivity study:* 5C*, 5 compartment head model with anisotropic white matter;* 4C*, 4 compartment isotropic head model and* 3C*, 3 compartment isotropic head model. The column indicates when the compartment has been split, e.g., brain compartment divided between white and gray matter; while the dash indicates that the relative compartment has been neglected in the head model.*

The anatomical data was anonimized and de-identified, i.e., facial details were removed from the T1w MRI. The defacing procedure from the *FieldTrip* (Oostenveld et al., 2011) routine and the resulting defaced MRI are visualized in Figure 2.1.

Once the anatomical data was defaced, a crucial step to construct the volume conduction head model was the segmentation of the anatomical data.

The goal of the segmentation is to classify each element of the anatomical image into specific tissue types, based on the intensity of the image, which relates to the conductivity of the corresponding tissue. The output of the head segmentation is a 3D matrix of label values identifying each homogeneous region. In our study, we considered five head compartments, namely, the scalp, the skull, the cerebrospinal fluid (CSF), the gray matter and the white matter.

As a consequence of the defacing step, the scalp layer produced by the automatized standard segmentation in FieldTrip had holes in the lower face area. We therefore manually corrected the segmentation by filling the holes in Seg3D (CIBC, 2016). Furthermore, we homogeneized the brain compartment in order to facilitate the segmentation procedure which follows. In Figure 2.2 the segmentation before and after manual correction are presented, while, in Figure 2.3, the final isosurfaces relative to the segmentation result are visualized.

As a next step, the segmentation result was used to produce a volumetric mesh.

In general, a volumetric mesh can be generated by tessellating the segmentation matrix usually with tetrahedral or hexahedral elements. In this study, we build two hexahedral mesh: one with 1 mm resolution, resulting in a mesh with $\approx$ 4,100 K nodes and $\approx$ 4,000 K hexahedra; and one with 2 mm resolution, resulting in a mesh with $\approx$ 350 K of nodes and $\approx$ 300 K hexahedra.

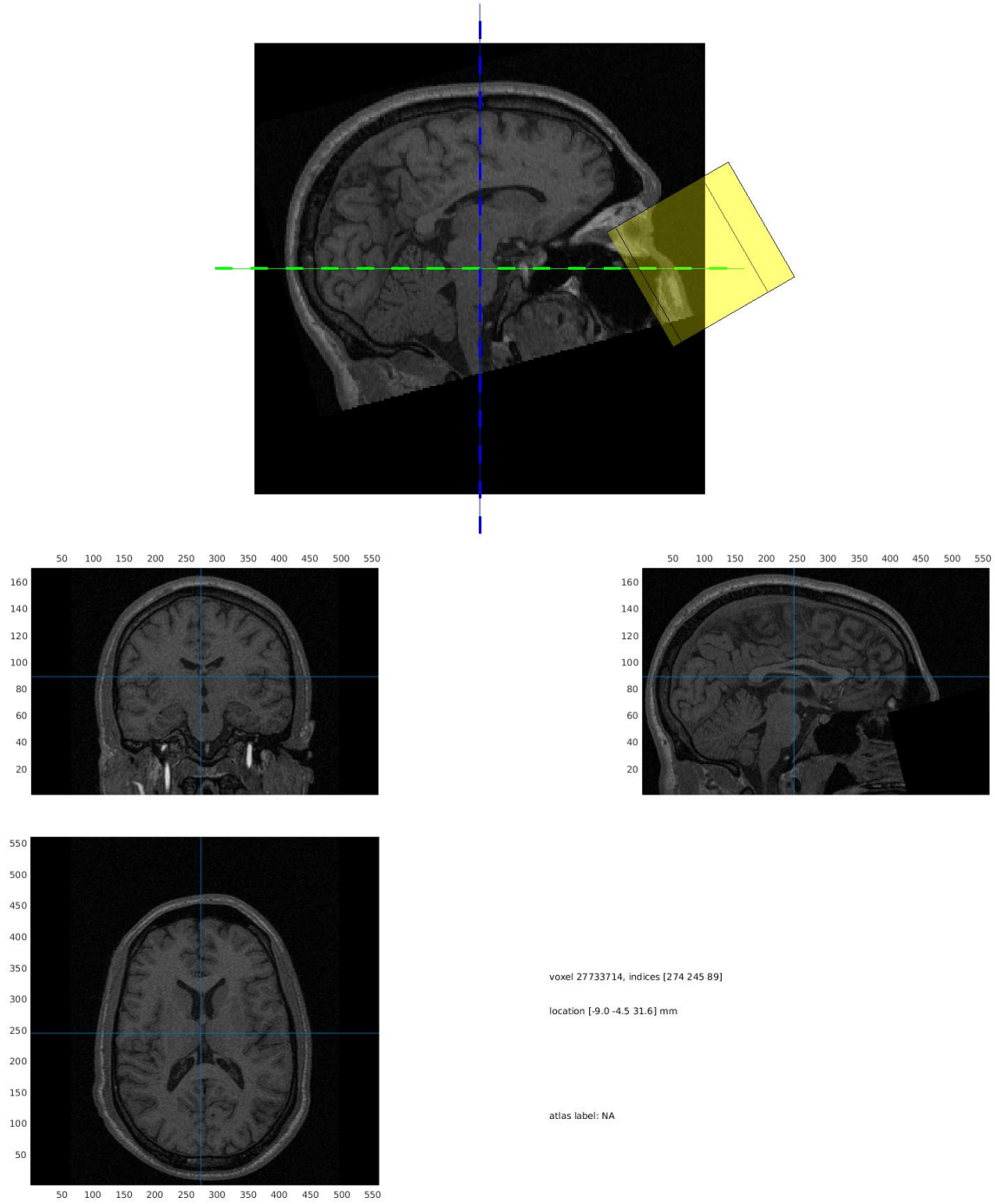

Figure 2.1 *Visualization of the defacing step included in FieldTrip (top) and the result of the deface procedure (bottom). The yellow box represents the area of the image which will be removed.*

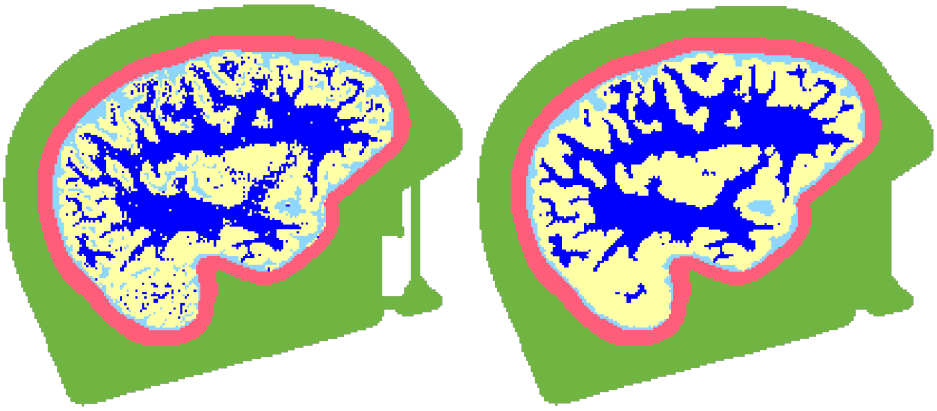

Figure 2.2 *Segmentation results before (on the left) and after (on the right) manual correction with Seg3D.*

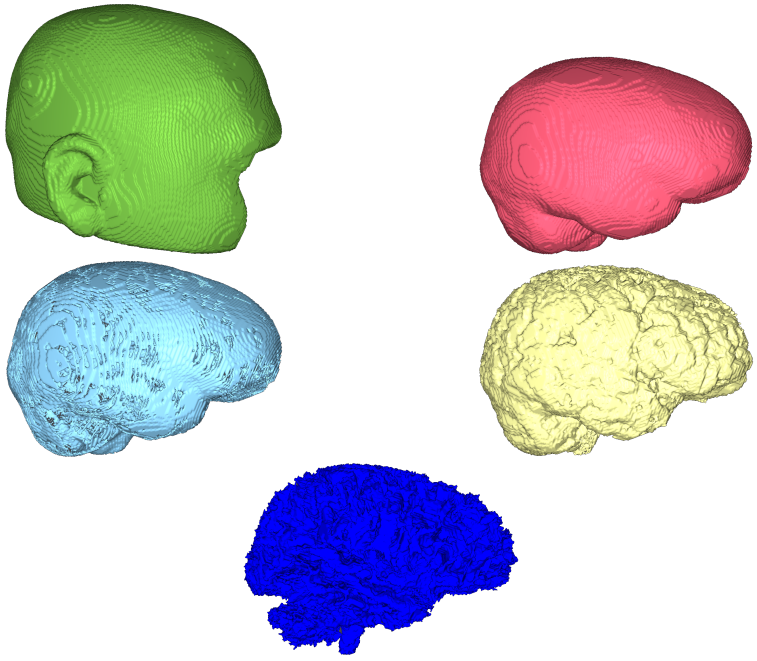

Figure 2.3 *Isosurfaces of the final segmentation results: scalp in green, skull in pink, CSF in light blue, gray matter in yellow and white matter in blue.*

In a tetrahedral mesh, the representation of surfaces is generally more accurate than the one in a hexahedral mesh, where stair-case scenarios may occur. In order to improve the accuracy of the surface representation in a hexahedral mesh, the nodes of each cube touching a conductivity jump were shifted by a factor of 0.3, as suggested, e.g., in (Vorwerk et al., 2018), and therefore the curvature of the surfaces were better emulated.

In the case of the (3C) and (4C) head models, only the labels were modified accordingly, while the mesh remained the same as the one for the (5C) head model, since the geometrical error was not studied in this work. The underlying mesh does not change when considering the different volume conduction head models, only the labels assigned to each cube of the mesh. The three head models are shown in Figure 2.4.

2.2 Continuous Galerkin FEM for Solving the (s)EEG Forward Problem

There are cases when the strong formulation is not adequate to model the physical phenomenon under examination. Therefore, strong assumption on the solution can be relaxed and the weak formulation is deduced, as already mentioned in Chapter 1.

Galerkin methods are approaches which can be adopted in order to discretize weak formulations, dealing therefore with discrete problems defined on finite-dimensional subspaces V_h of the test function space V, cfr. Chapter 1.

The finite element method in its simpler form is an example of a Galerkin method, as we will see in this chapter. The continuous Galerkin finite element method (CG-FEM) is also known as standard or Lagrangian FEM, as the function space V_h contains *Lagrangian* ansatz functions, i.e., *hat functions*. This function space constitutes a subset of $H^1(\Omega)$, therefore the method is said to be a *conforming* FEM.

In the discretization step the weak formulation becomes a linear system, the function space containing the solution and the test functions is finite-dimensional, and the problem is solved in a discretized domain as it is described in the following. The theory section mainly follows (Ciarlet, 2002) and (Quarteroni and Quarteroni, 2009).

In this chapter we deduce and illustrate the CG-FEM to solve the sEEG forward problem. To do so, we start (in Section 2.2.1) with the introduction of the basics of CG-FEM; in Section 2.2.2, the CG-FEM discretization scheme for the EEG forward solution is recalled throughout several representations of the right-hand side, namely, the *partial integration* approach (in

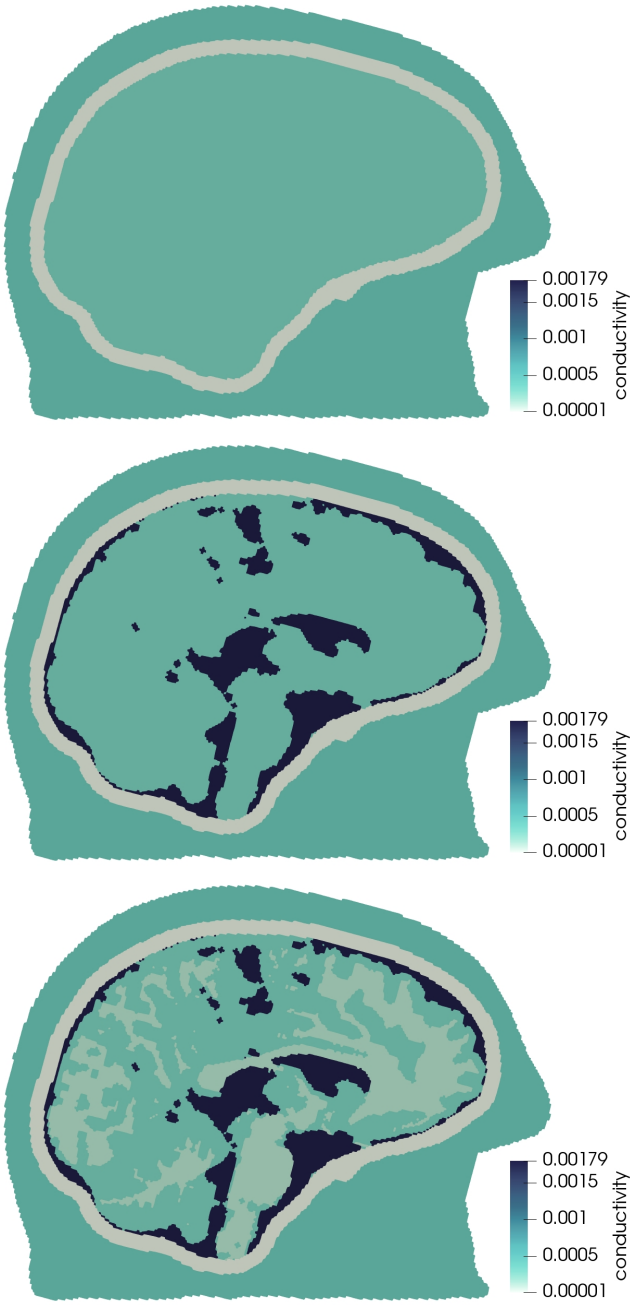

Figure 2.4 *Three 1 mm meshes representing the volume conduction head model: 3C (top), 4C (center), 5C (bottom). The color code follows the conductivity values.*

Section 2.2.4), the *subtraction* approach (in Section 2.2.3), and *Venant's* approach (in Section 2.2.5).

2.2.1 Basics of the CG-FEM

If we consider the abstract variational problem (cfr. Chapter 1): find $u \in V$ such that

$$a(u,v) = l(v), \forall v \in V, \tag{2.1}$$

posed over an open set Ω with a Lipschitz-continuous boundary, then the *Galerkin method* for approximating the solution of such problem consists in defining similar problems in finite-dimensional subspaces of the space V. More specifically, with a general finite-dimensional subspace V_h of V, we associate to (2.1) the discrete problem: find $u_h \in V_h$ such that

$$a(u_h, v_h) = l(v_h), \forall v_h \in V_h,$$

where u_h is the so-called discrete solution.
In order to apply the Galerkin method we therefore face, by definition, the problem of constructing finite-dimensional subspaces V_h of V. The finite element method, in its simplest form, is a specific process of constructing subspaces V_h, which shall be called finite element spaces. This construction is characterized by three basic aspects:

1. a triangulation $\mathscr{T}_h$ is established over the set $\bar{\Omega}$, i.e., the set $\bar{\Omega}$ is subdivided into a finite number of subsets E, called finite elements, in such a way that the following properties are satisfied:
   - $\bar{\Omega} = \bigcup_{E \in \mathscr{T}_h} E$
   - for each $E \in \mathscr{T}_h$, the set E is closed and the interior $\mathring{E}$ is non-empty
   - for each distinct $E_e, E_f \in \mathscr{T}_h$, one has $E_e \bigcap E_f = \emptyset$
   - for each $E \in \mathscr{T}_h$, the boundary ∂E is Lipschitz-continuous
2. the functions $v_h \in V_h$ are piecewise polynomials
3. there should exist a basis in the space V_h whose functions have *small* supports.

The CG-FEM is characterized by the following choice of V_h:

$$V_h = X_h^r = \{v_h \in \mathscr{C}^0(\Omega) : v_h|_E \in P_r, \forall E \in \mathscr{T}_h\}, \tag{2.2}$$

i.e., the space of functions which are globally continuous and piecewise polynomials. As in this case the space V_h is a subset of V, the CG-FEM is defined as a *conforming* FEM. We now introduce two particular polynomial spaces:

Definition 2.2.1. *(Polynomial space $\mathbb{P}_d^k$) Let $k \geq 0$ be an integer, $A_d^k := \left\{\alpha \in \mathbb{N}^d : |\alpha|_{l^1} \leq k\right\}$ and $|\cdot|_{l^1}$ the 1-norm. Then the polynomial space $\mathbb{P}_d^k$ of polynomials of d variables, of total degree at most k, is defined as*

$$\mathbb{P}_d^k := \left\{ p : \mathbb{R}^d \ni z \mapsto p(x) \in \mathbb{R} : \exists (\gamma_\alpha)_{\alpha \in A_d^k} \in \mathbb{R}^{card(A_d^k)} \text{ s.t. } p(x) = \sum_{\alpha \in A_d^k} \gamma_\alpha x^\alpha \right\}.$$

The dimension of $\mathbb{P}_d^k$ is equal to $card(A_d^k) = \binom{k+d}{k}$.

Definition 2.2.2. *(Polynomial space $\mathbb{Q}_d^k$) Let $k \geq 0$ be an integer, $B_d^k := \left\{\alpha \in \mathbb{N}^d : |\alpha|_{l^\infty} \leq k\right\}$ and $|\cdot|_{l^\infty}$ the ∞-norm. Then the polynomial space $\mathbb{Q}_d^k$ of polynomials of degree at most k in each variable is defined as*

$$\mathbb{Q}_d^k := \left\{ p : \mathbb{R}^d \ni z \mapsto p(x) \in \mathbb{R} : \exists (\gamma_\alpha)_{\alpha \in B_d^k} \in \mathbb{R}^{card(B_d^k)} \text{ s.t. } p(x) = \sum_{\alpha \in B_d^k} \gamma_\alpha x^\alpha \right\}.$$

The dimension of $\mathbb{Q}_d^k$ is equal to $card(B_d^k) = (k+1)^d$.

In the following, the space $P_r = \mathbb{P}_1^d$ is chosen when the triangulation is made of triangles ($d = 2$) or tetrahedra ($d = 3$) and $P_r = \mathbb{Q}_1^d$ when the triangulation is made of quadrilaterals ($d = 2$) or hexahedra ($d = 3$). In both cases, every function $v_h \in V_h$ is uniquely defined by the values that it assumes at the nodes $\mathbf{N}_i$, with $i = 1, ..., N_h$ of the triangulation $\mathcal{T}_h$. Therefore, a basis of V_h can be the set of functions $\varphi_j \in V_h$, $j = 1, ..., N_h$, such that

$$\varphi_j(\mathbf{N}_i) = \delta_{i,j} = \begin{cases} 0 & i \neq j \\ 1 & i = j \end{cases} \quad i, j = 1, ..., N_h.$$

In particular, if $r = 1$, the nodes are the vertices of the elements and the generic function φ_j is linear on each element, it is equal to 1 on node $\mathbf{N}_j$ and to 0 on every other node.
A generic function $v_h \in V_h$ can be expressed in terms of a linear combination of basis functions of V_h as follows

$$v_h(\mathbf{x}) = \sum_{i=1}^{N_h} v_i \varphi_i(\mathbf{x}), \ \forall \mathbf{x} \in \Omega, \tag{2.3}$$

where $v_i = v_h(\mathbf{N}_i)$.
In the following section, the CG-FEM discrete scheme for the EEG forward problem is recalled starting from the discretization just introduced. For further details see, e.g., (Vorwerk, 2016).

2.2.2 Solving the EEG Forward Problem

The conforming weak formulation of the EEG forward problem (1.9)-(1.10) introduced in Chapter 1 reads: find $u_h \in V_h \subset H^1(\Omega)$ such that

$$\int_\Omega \sigma \nabla u_h \cdot \nabla v_h dx = \int_\Omega f v_h dx \tag{2.4}$$

holds true, $\forall v_h \in V_h$. Choosing V_h as the space of piecewise linear, continuous functions, i.e., $V_h = X_h^r$, results in the classical CG-FEM. If we express the discrete solution u_h of (2.4) in terms of the basis $\{\varphi_j\}_j$ by using (2.3), we obtain

$$u_h(\mathbf{x}) = \sum_{j=1}^{N_h} u_j \varphi_j(\mathbf{x}), \ \forall \mathbf{x} \in \Omega, \tag{2.5}$$

where $u_j = u_h(\mathbf{N}_j)$. If we assume that (2.5) satisfies (2.4) for each element of the basis, then we obtain the following linear system with N_h equations in the N_h unknowns u_j which is equivalent to the problem (2.4),

$$\sum_{j=1}^{N_h} u_j \int_\Omega \sigma \nabla \varphi_j \cdot \nabla \varphi_i dx = \int_\Omega f \varphi_i dx, \tag{2.6}$$

for $i = 1, ..., N_h$. (2.6) can also be rewritten in terms of a discretized version of the bilinear and linear form a and l, i.e., a_h and l_h, respectively, as follows

$$a_h(\varphi_i, \varphi_j) = l_h(\varphi_i).$$

The so-called *stiffness matrix* of dimensions $N_h \times N_h$ is defined as

$$A = (a_{i,j})_{i,j=1,...,N_h}, \tag{2.7}$$

where

$$a_{i,j} = a_h(\varphi_i, \varphi_j) = \int_\Omega \sigma \nabla \varphi_j \cdot \nabla \varphi_i dx,$$
$$l_i = l_h(\varphi_i) = \int_\Omega f \varphi_i dx.$$

If we furthermore introduce the vectors:

$$\mathbf{u} = (u_j)_j,\ \mathbf{l} = (l_i)_i,$$

the linear system in (2.6) can be written as follows

$$A\mathbf{u} = \mathbf{l}. \tag{2.8}$$

As the support of the generic basis function φ_i is made of only the elements of the triangulation which share the node $\mathbf{N}_i$, the matrix A is sparse. In our work, the linear system (2.8) is solved by means of a preconditioned conjugate gradient (CG) solver, more specifically with the algebraic multi-grid (AMG) preconditioning. The AMG-CG solver was already implemented in the Distributed and Unified Numerics Environment (DUNE) [1] (Bastian and Blatt, 2007; Bastian et al., 2008a,b).

Remark 1. *When defining the vector $\boldsymbol{l}$, we did not consider the fact that often a dipolar expression of the source is taken into account. Therefore the integral in l_i is in general not well-defined when $f = \nabla \cdot \boldsymbol{j}^p = \nabla \cdot \boldsymbol{M}\delta_{\boldsymbol{r}_0}$.*

In the following sections three strategies adopted to deal with the singularity in l_i are described.

2.2.3 The Subtraction Approach

As already mentioned, the mathematical point dipole model introduces a singularity on the right-hand side of the PDE in (1.9) that can be treated, for example, with the so-called subtraction approach (Awada et al., 1997; Bertrand et al., 1991; Drechsler et al., 2009; Marin et al., 1998; Wolters et al., 2007).
The subtraction approach assumes that a non-empty neighborhood Ω^∞ around the source in $\mathbf{r}_0$ can be found with homogeneous conductivity σ^∞. The conductivity tensor σ is then split

[1] http://www.dune-project.org

into two parts,

$$\sigma = \sigma^{\infty} + \sigma^{corr}, \tag{2.9}$$

where σ^{corr} vanishes in Ω^{∞}. The potential u can also be split into two contributions,

$$u = u^{\infty} + u^{corr}. \tag{2.10}$$

The so-called *singularity potential* u^{∞} is the solution of the Poisson equation in an unbounded and homogeneous conductor with constant conductivity σ^{∞}, and it can be computed analytically, see e.g. (Drechsler et al., 2009). The *correction potential* u^{corr} becomes the unknown of a new Poisson equation:

$$-\nabla \cdot (\sigma \nabla u^{corr}) = \nabla \cdot (\sigma^{corr} \nabla u^{\infty}), \qquad \text{in } \Omega \subseteq \mathbb{R}^3 \tag{2.11}$$

$$\sigma \nabla u^{corr} \cdot \mathbf{n} = -\sigma \nabla u^{\infty} \cdot \mathbf{n}, \qquad \text{on } \partial\Omega \tag{2.12}$$

after embedding (2.9) and (2.10) in (1.9) and (1.10). The conforming weak formulation of (2.11)-(2.12) presented in (Wolters et al., 2007) reads: find $u_h^{corr} \in V_h \subset H^1(\Omega)$ such that

$$\int_{\Omega} \sigma \nabla u_h^{corr} \cdot \nabla v_h dx = -\int_{\Omega} \sigma^{corr} \nabla u_h^{\infty} \cdot \nabla v_h dx - \int_{\partial\Omega} \sigma^{\infty} \nabla u^{\infty} \cdot \mathbf{n} \, v_h ds \tag{2.13}$$

holds true, $\forall v_h \in V_h$. When choosing V_h as the space of piecewise linear, continuous functions the classical CG-FEM is obtained.

The subtraction approach is theoretically well understood. A deep numerical analysis of the subtraction approach including proofs for uniqueness and existence has been carried out in (Wolters et al., 2007) and (Drechsler et al., 2009).

The matrix form of (2.13) is: find $u_h^{corr} \in V_h$ such that

$$A\mathbf{u}^{corr} = \mathbf{l}^{corr}, \tag{2.14}$$

where A is the stiffness matrix defined in (2.7), $\mathbf{u}^{corr} = (u_j^{corr})_j$, and $\mathbf{l}^{corr} = (l_i^{corr})_i = -\int_{\Omega} \sigma^{corr} \nabla u^{\infty} \cdot \nabla \varphi_i dx - \int_{\partial\Omega} \sigma^{\infty} \nabla u^{\infty} \cdot \mathbf{n} \varphi_i ds$. Once the linear system (2.14) is solved, the full potential $u_h = u_h^{corr} + u^{\infty}$ can be assembled.

Remark 2. *When the subtraction approach is adopted for discretizing the EEG forward problem, two main points have to be considered:*

1. *the numerical accuracy of the method for sources that are very close to a conductivity jump, e.g., the brain-CSF boundary, can decrease remarkably (see (Wolters et al., 2007) and (Drechsler et al., 2009));*

2. *the discrete right-hand side of the linear system is a dense vector, therefore the computation can be time-consuming.*

2.2.4 The Partial Integration Approach

Another way to deal with the singular right-hand side of the EEG forward problem equation is to use the definition of a differential operator D acting on the Dirac delta distribution centered in $\mathbf{r}_0 \in \mathbb{R}^3$, i.e.,

$$\langle D(\delta_{\mathbf{r}_0}), \phi \rangle = -D(\phi)(\mathbf{r}_0), \tag{2.15}$$

where ϕ is a smooth function with compact support. If we use this definition on the right-hand side of (2.4) with $D = \nabla$, we obtain

$$\begin{aligned} l(v_h) &= \int_\Omega f v_h dx \\ &= \int_\Omega \nabla \cdot (\mathbf{M}\delta_{\mathbf{r}_0}) v_h dx \\ &= -\mathbf{M}\nabla v_h(\mathbf{r}_0), \end{aligned}$$

where we considered the fact that $\mathbf{M}$ is constant and the behavior of the delta distribution and the integral operator.
The name of this approach comes from the fact that definition (2.15) mimics Gauss' theorem, or *partial integration*, for multi-dimensional functions. The discrete right-hand side of the linear system in (2.6) therefore is

$$\mathbf{l} = (l_i)_i = (-\mathbf{M}\nabla\varphi_i(\mathbf{r}_0))_i.$$

The vector $\mathbf{l}$ has non-zero entries only in the support of the basis function φ_i which contains the dipole itself. Furthermore we notice that in case of $V_h = \mathbb{P}_1$, l_i is constant on each element of the triangulation $\mathscr{T}_h(\Omega)$.

2.2.5 Venant's Approach

A third strategy to deal with the singular right-hand side of (2.4) makes use of the principle of Saint-Venant, and we refer to it as Venant's approach. Barré de Saint-Venant formulated

his famous principle in 1855, but it was more of an observation than a strict mathematical statement: "If the forces acting on a small portion of the surface of an elastic body are replaced by another statically equivalent system of forces acting on the same portion of the surface, this redistribution of loading produces substantial changes in the stresses locally, but has a negligible effect on the stresses at distances which are large in comparison with the linear dimensions of the surface on which the forces are changed"(Barr de Saint-Venant, 1853).

Many scientists gave a more rigorous formulation of the principle, mainly in applications of elasticity. In structural engineering this principle is extensively used and the main message is that the exact distribution of a load is not important far away from the loaded region, as long as the resultants of the load are correct. This principle can be applied also in electrostatics, where instead of loads we deal with charges, and the resultants of the loads are the moments of the electric source distribution. Therefore, a point dipole can be replaced by a distribution of electrical monopoles, as long as the moments are equivalent. Crucial issues to address are related to the choice of the position and the intensity of the charges. (Buchner et al., 1997), together with (Medani et al., 2015; Vorwerk, 2016; Wolters et al., 2007), dealt with these issues and here the main steps are reported.

The choice of the charge positions relies on the fact that we are considering Lagrangian finite elements and the associated Lagrangian ansatz functions, whose degrees of freedom are the values of the basis functions at the nodes of the triangulation. Hence, the monopoles are placed on the nodes of the element which contains the dipolar source. With regard to the choice of charge intensities, a linear system is built, where the actual moments of the dipolar source are equalized to the ones of a discrete distribution of electrical monopoles. More details are in the following.

The moments of a dipolar source are defined as

$$ {}^{k}T = Q\left(\frac{d}{2}\right)^{k} - Q\left(\frac{-d}{2}\right)^{k} = Q\frac{d^{k}}{2}\,(1-(-1)^{k}), $$

where Q is the charge strength, d is the distance between the two monopoles constituting the dipole, i.e., a source and a sink of equal strength Q. If the dipole is placed at the i-th node, we can write its target dipole moment as ${}^{k}T_{i}^{j}$, with $j = 1,2,3$. On the other side, the moments of a source distribution at an observation point $\mathbf{r}$ are defined as

$$ {}^{k}M(\mathbf{r}) = \int_{\Omega} (\mathbf{r}' - \mathbf{r})^{k} \rho(\mathbf{r}') d^{3}\mathbf{r}', $$

where ρ is the continuous distribution of charge. When a point-like monopolar distribution of charge is considered, i.e., when

$$\rho(\mathbf{r}) = \sum_{l=1}^{N} q_l \delta(\mathbf{r} - \mathbf{r}_l),$$

where q_l are the monopolar source strengths and $\mathbf{r}_l$ are the locations of the monopoles, we get the moments

$$^{k}M(\mathbf{r}) = \sum_{i=l}^{N} (\mathbf{d}_l)^k q_l, \tag{2.16}$$

where $\mathbf{d}_l = \mathbf{r} - \mathbf{r}_l$. If we refer to monopolar load moment for the k-th monopole close to the i-th monopole, we write $^{k}M_i^j$, and the distances become $(\mathbf{d}_{il})_j^k$, with $j = 1,2,3$. The vector equation (2.16) can be written as a linear system, which we express for every component $j = 1,2,3$ of the vectors in (2.16):

$$\begin{bmatrix} (^0M_i)_j \\ (^1M_i)_j \\ \vdots \\ (^kM_i)_j \end{bmatrix} = \begin{bmatrix} (\mathbf{d}_{i,1})_j^0 & (\mathbf{d}_{i,2})_j^0 & \cdots & (\mathbf{d}_{i,N})_j^0 \\ (\mathbf{d}_{i1})_j^1 & (\mathbf{d}_{i2})_j^1 & \cdots & (\mathbf{d}_{iN})_j^1 \\ \vdots & \vdots & \ddots & \vdots \\ (\mathbf{d}_{i1})_j^k & (\mathbf{d}_{i2})_j^k & \cdots & (\mathbf{d}_{iN})_j^k \end{bmatrix} \cdot \begin{bmatrix} q_1 \\ q_2 \\ \vdots \\ q_N \end{bmatrix}.$$

In the next step, a quadratic positive functional $D > 0$ is introduced and minimized, in the spirit of a least squares expression and inverse regularization techniques.

$$D = \frac{1}{2}\left(^{k}T_i^j - (d_{il}^j)^k q_l\right)\left(^{k}T_i^j - (d_{is}^j)^k q_s\right) + \lambda_D \frac{1}{2} q_l g_{ls} q_s,$$

where

$$g_{ls} = \begin{cases} (d_{il} d_{is}) & l = s \\ 0 & l \leq s. \end{cases}$$

When differentiating with regard to q_t we obtain

$$\left((d_{it}^j)^k (d_{is}^j)^k + \lambda_D g_{ts}\right) q_s = (d_{it}^j)^{kk} T_i^j,$$

which can be rewritten as

$$a_{ts} \cdot \mathbf{q}_s = \mathbf{b}_t. \tag{2.17}$$

The system (2.17) is symmetric and positive definite and the order is given by the number of monopoles, which are chosen, for example, as the nodes belonging to the same element

as the dipolar source, therefore the system can be solved fast. For further details about this approach and for the discussion about the choice of the parameters involved, we refer to (Buchner et al., 1997). Finally, the right-hand side of (2.4) looks like

$$\mathbf{l} = (l_i)_i = (\mathbf{q}_i)_i,$$

which is different from zero only in the neighboring nodes of the source location.

2.3 Discontinuous Galerkin FEM for Solving the (s)EEG Forward Problem

The discontinuous Galerkin finite element method (DG-FEM) originates from the idea of including boundary conditions in the weak formulation of a partial differential equation (PDE) via Nitsche's method (Nitsche, 1971), instead of restricting the test function space. The main idea of DG-FEM is an extension of this concept, namely, translating conservation properties into penalty terms in the weak formulation of a PDE. A DG-FEM forward modeling approach has recently been proposed for solving the EEG forward problem by (Engwer et al., 2017). We recall some main properties of DG-FEM for the EEG.

First, we recall the volume triangulation $\mathscr{T}_h(\Omega)$ introduced in 2.2.1, which is a a finite collection of disjoint and open subsets forming a partition of the domain Ω, where $h \in \mathbb{R}$ corresponds to the mesh-width. Furthermore, the triangulation induces the *internal skeleton*

$$\Gamma_{int} \coloneqq \left\{ \gamma_{e,f} = \partial E_e \cap E_f | E_e, E_f \in \mathscr{T}_h(\Omega), E_e \neq E_f, |\gamma_{e,f}| > 0 \right\} \tag{2.18}$$

and the *skeleton* $\Gamma \coloneqq \Gamma_{int} \cup \partial\Omega$. Let Y_h^r be the so-called *broken polynomial space*, that is defined as piecewise polynomial space on the partition $\mathscr{T}_h(\Omega)$:

$$Y_h^r \coloneqq \{ v \in L^2(\Omega) : v|_E \in P_r(E), \forall E \in \mathscr{T}_h(\Omega) \}, \tag{2.19}$$

where P_r denotes the space of polynomial functions of degree $r \in \mathbb{N}$. They describe functions that exhibit element-wise polynomial behavior but may be discontinuous across element interfaces.

In the following we assume that the conductivity tensor σ is constant on each element E_i and denote its value by σ_i.

Note the difference between the CG-FEM function space X_h^r defined in (2.2) and Y_h^r in

(2.19). While in (2.2) functions are globally continuous and locally, i.e., on each element, polynomial, the space defined in (2.19) contains globally L^2 functions which are not globally continuous.
Furthermore, we recall the definition of the *jump* of a function $u \in Y_h^r$ on the intersection between two elements E_e and E_f of the triangulation $\mathscr{T}_h(\Omega)$ with outer normal $\mathbf{n}_e \in \mathbb{R}^3$ and $\mathbf{n}_f \in \mathbb{R}^3$, respectively:

$$[\![u]\!] \coloneqq u|_{E_e}\mathbf{n}_e + u|_{E_f}\mathbf{n}_f \in \mathbb{R}^3.$$

Note that the normals $\mathbf{n}_e$ and $\mathbf{n}_f$ are opposing vectors, i.e. $\mathbf{n}_e = -\mathbf{n}_f$. In addition, the *weighted average* of u on the interface is defined as

$$\{u\} \coloneqq \frac{\sigma_f}{\sigma_e + \sigma_f} u|_{E_e} + \frac{\sigma_e}{\sigma_e + \sigma_f} u|_{E_f}.$$

Finally, we recall the following property:

$$[\![uv]\!] = [\![u]\!]\{v\} + \{u\}[\![v]\!]. \tag{2.20}$$

For more details we refer, e.g., to (Engwer et al., 2017).

2.3.1 Solving the EEG Forward Problem

In the DG-FEM context, the strategy to derive the weak form of the EEG forward problem is to first divide the whole domain Ω into elements of the triangulation $\mathscr{T}_h$, and then apply Gauss' theorem locally, on each element of the triangulation, where the discrete test and ansatz functions are polynomials (see (2.19)).

In (Engwer et al., 2017), the *symmetric interior penalty Galerkin* (SIPG) DG discretization for (1.9)-(1.10) is obtained, and it reads: find $u_h \in Y_h^r$ such that

$$a_h(u_h, v_h) + J_h(u_h, v_h) = l_h(v_h), \ \forall v_h \in Y_h^r, \tag{2.21}$$

with

$$\begin{aligned} a_h(u_h, v_h) = &\int_\Omega \sigma \nabla_h u_h \cdot \nabla_h v_h \, \mathrm{d}x - \int_{\Gamma_{int}} \{\sigma \nabla_h u_h\} \cdot [\![v_h]\!] \, \mathrm{d}s \\ &- \int_{\Gamma_{int}} \{\sigma \nabla_h v_h\} \cdot [\![u_h]\!] \, \mathrm{d}s, \end{aligned}$$

$$J_h(u_h, v_h) = \eta \int_{\Gamma_{int}} \frac{\hat{\sigma}_\gamma}{h_\gamma} [\![u_h]\!] \cdot [\![v_h]\!] \, \mathrm{d}s,$$

and

$$l_h(v_h) = \int_\Omega f v_h \, \mathrm{d}s,$$

where η indicates the penalty parameter (which has to be chosen large enough to ensure coercivity), $\hat{\sigma}_\gamma$ and h_γ denote local definitions of the mesh width and the electric conductivity on an edge γ, respectively. In this particular case, $\hat{\sigma}_\gamma$ is chosen according to (Di Pietro et al., 2008) and h_γ as the harmonic average of the conductivities of the adjacent elements (Giani and Houston, 2011):

$$\hat{\sigma}_{\gamma_{e,f}} := \frac{min\left(|E_e|, |E_f|\right)}{|\gamma_{e,f}|},$$

and

$$h_{\gamma_{e,f}} := \frac{2\sigma_e \sigma_f}{\sigma_e + \sigma_f}.$$

The proposed discretization (2.21) is consistent and adjoint-consistent with the strong problem (1.9)-(1.10), and for a sufficiently large constant $\eta > 0$ it has a unique solution. Further details and proofs are in (Engwer et al., 2017).

Remark 3. *In the DG discretization we make use of the so-called piecewise gradient, ∇_h, which is defined in the interior of each element in the volume triangulation $\mathscr{T}_h(\Omega)$. It holds that*

$$\nabla_h v_h = \nabla(v_h|_K), \ \forall v_h \in Y_h^r. \tag{2.22}$$

In following, when no ambiguity arises, we will use ∇, $a(\cdot,\cdot)$, $J(\cdot,\cdot)$, $l(\cdot)$, Γ_{int}, instead of ∇_h, $a_h(\cdot,\cdot)$, $J_h(\cdot,\cdot)$, $l_h(\cdot)$, Γ_{int}^h, respectively.

2.3.2 The Discrete Conservative Flux

In the continuum, the strong formulation of Poisson's equation, which we recall here:

$$\begin{aligned} \nabla \cdot (\sigma \nabla u) &= \nabla \cdot \mathbf{j}^p, && \text{in } \Omega \subseteq \mathbb{R}^3 \\ \sigma \nabla u \cdot \mathbf{n} &= 0, && \text{on } \partial\Omega \end{aligned}$$

leads to a conservation of charge property:

$$\int_{\partial K} (\sigma \nabla u) \cdot \mathbf{n} \, \mathrm{d}s = \int_K f \, \mathrm{d}x, \ \forall K \subset \Omega, \tag{2.23}$$

where $f = -\nabla \cdot \mathbf{j}^p$ and K is a control volume in Ω.

We can point out that in the current setting, the current $\mathbf{j}$ is solenoidal, or diverge-free, hence it holds that

$$\int_{\partial K} \nabla \cdot (\mathbf{j}^s + \mathbf{j}^p)\,\mathrm{d}x = 0,\ \forall K \subset \Omega. \tag{2.24}$$

We have already mentioned in Section 1.3.2 that for FEMs the conservation of charge property carries over to the discrete solution only if the test space contains the characteristic function, which is one in K and zero everywhere else. In general, a conforming discretization, like CG-FEM, does not guarantee this property, while the DG-FEM fulfills a discrete analogue, as we see in the following.

In order to deduce the DG discrete conservation property, the strategy is to test the strong formulation with an *indicator* function χ_K which is defined as

$$\chi_k(\mathbf{x}) \coloneqq \begin{cases} 1 & \text{if } \mathbf{x} \in K \\ 0 & \text{otherwise} \end{cases}$$

where K is a control volume in Ω, i.e., $K \in \mathscr{T}_h(\Omega)$. Note that $\chi_K \in Y_h^r$.

When we plug-in χ_k in (2.21), we have:

$$a_h(u_h, \chi_k) + J_h(u_h, \chi_k) = l_h(\chi_k),$$

which is equivalent to

$$\int_{\partial K} \left(\{\sigma \nabla u_h\} - \eta \frac{\hat{\sigma}_\gamma}{h_\gamma} [\![u_h]\!] \right) \mathbf{n}_K \,\mathrm{d}s = \int_K f \,\mathrm{d}x,$$

exploiting the following facts:

1. $\nabla \chi_k$ denoted here $\nabla_h \chi_k = \nabla(\chi_k|_K) = 0$;
2. $[\![\chi_k]\!] = \chi_k|_K \mathbf{n}_K = \mathbf{n}_K$.

2.4 Stereo EEG Data

The sEEG data of one epileptic patient consists in uninterrupted recording of 67.30 seconds, acquired with sEEG amplifier system (NIHON-KOHDEN NEUROFAX-110) at a sampling rate of 1 kHz. During this time interval when 29 electric pulses of 5 mA are injected in the anode (K6) and extracted in the cathode in contact K5. Before stereotactic electrode

implantation, the subjects gave written informed consent for participation in research studies and for publication of data. This study was approved by the ethical committee of the Niguarda "Ca' Granda" Hospital, Milan.

SEEG data are measured through platinum–iridium semi–flexible multilead intracerebral electrodes, with a diameter of 0.8 mm, a contact length of 2 mm, an inter–contact border-to-border distance of 1.5 mm (Dixi Medical, Besancon, France). The anatomical positions and amounts of electrodes varied according to surgical requirements (Cardinale et al., 2012). The patient whose data we analyzed was implanted with 14 shafts, namely, 11 in the right hemisphere and 3 in the left hemisphere, with 18 contacts per shaft.

Chapter 3

Validation Approach

The proposed validation approach consists in several steps which will be illustrated in this chapter. The general idea of this approach is to compare the actual measured potentials with the simulated potentials in each of the three volume conduction head models (3C, 4C and 5C) during the stimulation sessions.

3.1 Extraction of the Contact Positions

Stereo-EEG data are measured through platinum–iridium semi–flexible multilead intracerebral electrodes, with a diameter of 0.8 mm, a contact length of 2 mm, an inter–contact border-to-border distance of 1.5 mm (Dixi Medical, Besancon, France). The anatomical positions and amounts of electrodes varied according to surgical requirements (Cardinale et al., 2012). The patient whose data we analyzed was implanted with 14 shafts, namely, 11 in the right hemisphere and 3 in the left hemisphere, with 18 contacts per shaft. In Figure 3.1 all the contacts are visualized.

Note that in this study we did not take into account the exact geometry of the contacts and the shafts. Moreover we did not consider the electrical features, i.e., the impedance, of the material constituting the shafts/contacts. (von Ellenrieder et al., 2012) investigated the sensitivity of depth electrodes with different contact sizes and for different values of the contact impedance, and they found that it is not necessary to include detailed electrode models in volume conduction problems such as the stereo-EEG forward and inverse problems.

The contacts are therefore considered to be point-contacts and are depicted with sphere in Figure 3.1.

In order to get those locations, the post-implant CT image was segmented and the electrode positions were extracted by using the method described in (Arnulfo et al., 2015a),

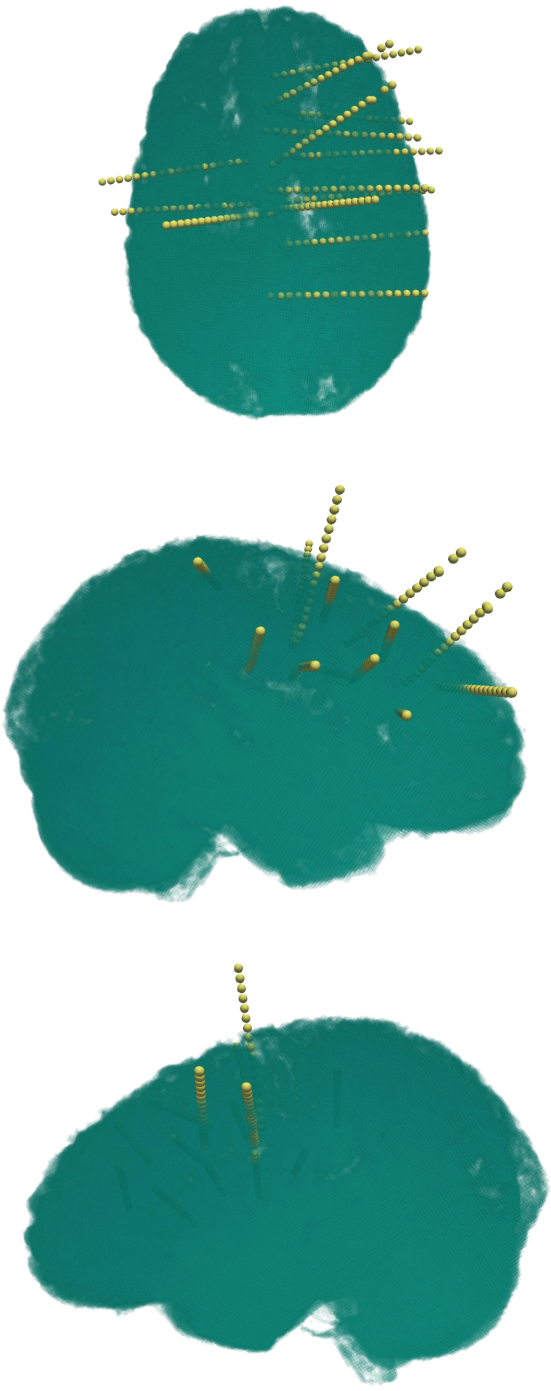

Figure 3.1 *Brain compartment (in blue) visualized together with all the 252 contacts (yellow spheres) in an axial and two sagittal planes.*

and the tool described in (Arnulfo et al., 2015b; Narizzano et al., 2017). In (Narizzano et al., 2017), SEEG Assistant is presented a set of tools integrated in a single 3DSlicer extension, which aims to assist neurosurgeons in the analysis of post-implant structural data and hence aid the neurophysiologist in the interpretation of SEEG data.

3.2 Dipolar Source Model

As we have already seen in Chapter 1, main ingredients for forward problem simulations are: the volume conduction head models, which were described in details in Chapter 2; the sensor model, which was explained in Section 3.1; the numerical method to solve the partial differential equation, extensively introduced in Chapter 2; and the source model. In this Section we will discuss about the latter.

The provided sEEG data consists in 67.30 seconds where the couple of contacts K6 - K5 were used as anode and cathode, respectively. A current of 5 mA was injected in K5 and collected in K6. Since the distance between each contact is two orders of magnitude lower than the whole head size and it is well known that an electric dipole field attenuates with the inverse of the squared distance (see, for example, (Hallez et al., 2007)), it is reasonable to model the injected current as the one generated by a point dipole.

Therefore, we placed a unitary dipole in the midpoint between K5 and K6, with the orientation given by the K-shaft orientation and the direction going from the cathode (K6) to the anode (K5). The dipole direction is indeed opposite the current orientation.

3.3 FEM Simulations

Once the volume conduction head model, the sensor model and the dipole model have been built, we computed a CG-FEM solution with the *duneuro* software (Nüßing et al., 2019) via the python interface (see [1] for more details on the code utilized).

The simulations took below the minute for the CG-FEM computation.

In Figure 3.2, the simulated electric current are visualized in the three head models, when the partial integration approach and a 1 mm mesh ware adopted.

[1] http://www.duneuro.org

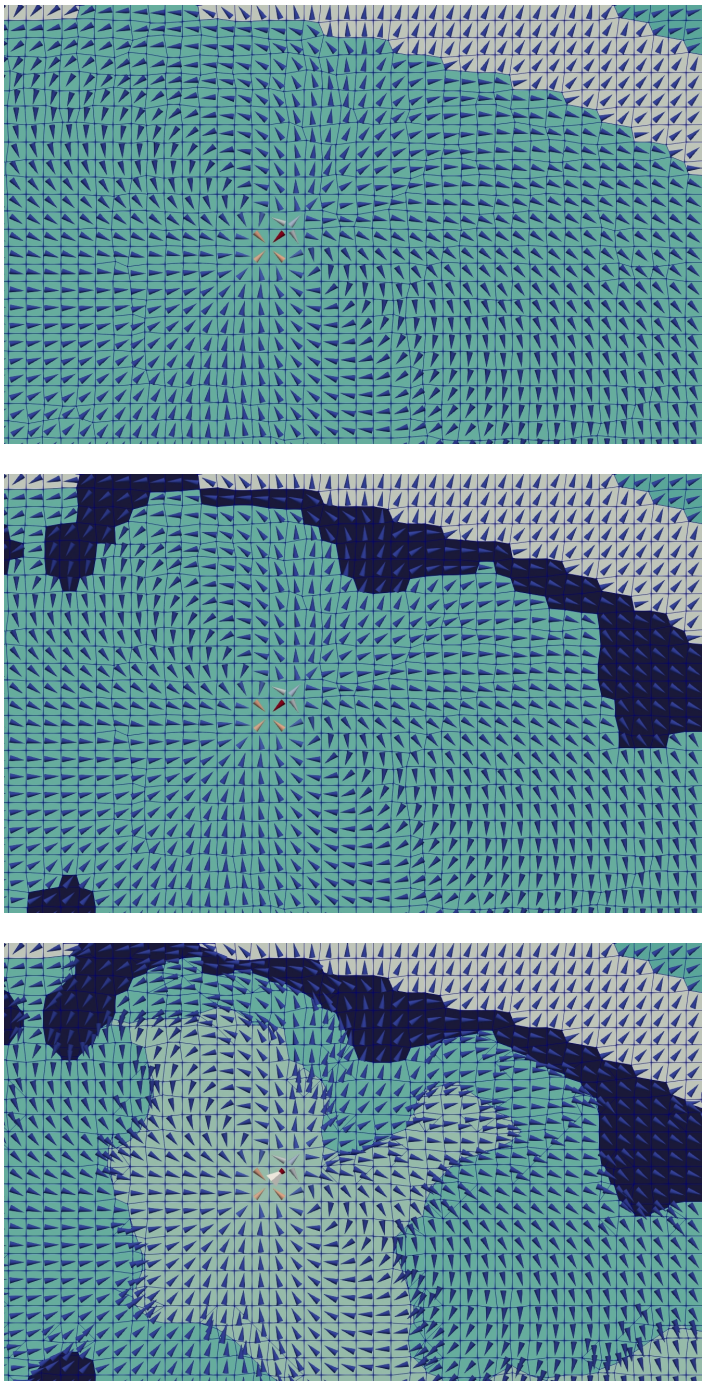

Figure 3.2 *Visualization of simulated electric current in 3C (top), 4C (center) and 5C (bottom) on a coronal plane of the volume conduction head model. Overlaid to the potentials are the conductivity profile values. The cones depict the electric current.*

3.4 sEEG Data Analysis

The sEEG data of one epileptic patient consists in uninterrupted recording of 67.30 seconds, acquired with sEEG amplifier system (NIHON-KOHDEN NEUROFAX-110) at a sampling rate of 1 kHz. During this time interval when 29 electric pulses of 5 mA are injected in the anode (K5) and extracted in the cathode in contact K6.

The provided data are relative to the contacts inside the brain compartment only, namely 186 contacts.

First of all we visually inspected the data and removed the electrodes close to the dipole position, i.e., the anode, the cathode and the direct neighbors.

In this analysis, we did not consider also the contacts with the following labels: 'FZ', 'CZ', 'E', 'KG', 'DEL1-4', 'DC09', 'EEGMark1-2', 'TIB1-4', 'MILO1-2', 'EOG1-2'.

Second, we re-referenced the data following two different schemes: monopolar (MP) and bipolar (BP).

Monopolar In case of the MP reference, we identified the contact in the white matter whose distance from the dipole position was the maximum. The identified electrode is 'R12' with a distance of 40.8 mm.

We then re-referenced the data to 'R12', by subtracting the signal relative to 'R12' to the signal relative to all the other contacts.

Bipolar In the case of BP reference, we subtracted the signal relative to neighbor contacts, per each shaft. We avoided contacts which where more than 3.5 mm far away from each other, i.e., we considered only contiguous contacts when subtracting the signals.

Once the data had been re-referenced, we performed a baseline correction, selecting the baseline window of the first 12 ms of the recording, far away from the first electric stimulation.

We identified the 29 peaks corresponding to the 29 electric stimulations, for each contact. Finally, we computed the mean peak value among the 29 peaks. The peaks do not appear to have the same amplitude, and as the signal is two orders of magnitude higher than the biophysiological signal, the peak amplitude difference is not due to volume conduction effects, but it might be caused, for example, by a lower sampling rate than the pulse itself.

Finally, we wrote the mean peaks at each recording point-contact into vtk files to facilitate the comparisons conducted in the following Section.

3.5 Results

In this Section we present the results of the comparison between measured data and simulated data when three different compartment head models are used with the CG-FEM scheme implemented in *duneuro* (Nüßing et al., 2019), for three different source model, namely, partial integration (PI), subtraction approach (SA) and Venant's approach (VEN), and for both mesh resolutions, i.e., 2 mm and 1 mm.

The error measure we adopted is the relative error in percentage, i.e.,

$$RE\%(i) = \left| \frac{|\mathbf{m}(i)| - |\mathbf{s}(i)|}{|\mathbf{m}(i)|} \right|, \tag{3.1}$$

for the ith contact, where $\mathbf{m}$ represents the measured potential difference and $\mathbf{s}$ represents the simulated potential difference. In the following, boxplot of the relative errors, together with head model visualizations are shown.

Furthermore, when analyzing the shafts independently, we computed the topographical error in percentage, i.e.,

$$RDM\%(\mathbf{m},\mathbf{s}) = 50 \left\| \frac{\mathbf{m}}{\|\mathbf{m}\|_2} - \frac{\mathbf{s}}{\|\mathbf{s}\|_2} \right\|_2, \tag{3.2}$$

and the magnitude error in percentage, i.e.,

$$MAG\%(\mathbf{m},\mathbf{s}) = 100 \left(\frac{\|\mathbf{s}\|_2}{\|\mathbf{m}\|_2} - 1 \right). \tag{3.3}$$

3.5.1 Single Shaft Comparison Results

In this subsection, we present the comparison results where we analyzed single shafts.

First, we visualized in Figure 3.3 the simulated potentials computed with CG-FEM implemented in *duneuro* (Nüßing et al., 2019) in the three different volume conduction head models together with the measured responses with the MP reference scheme.

In Figure 3.3, the modulation of the different conductivity profile is visible. In particular, we notice how the skull and the CSF have different effects on the potential distribution: while the skull compartment acts as an isolator (the skull conductivity is the lowest in the models, see Table 2.1), the CSF compartment, which has the highest conductivity in the model, leads to shunting effects.

From Figure 3.3 we see a clear match in pattern between simulated and measured potential, even though a magnitude shift is remarkable.

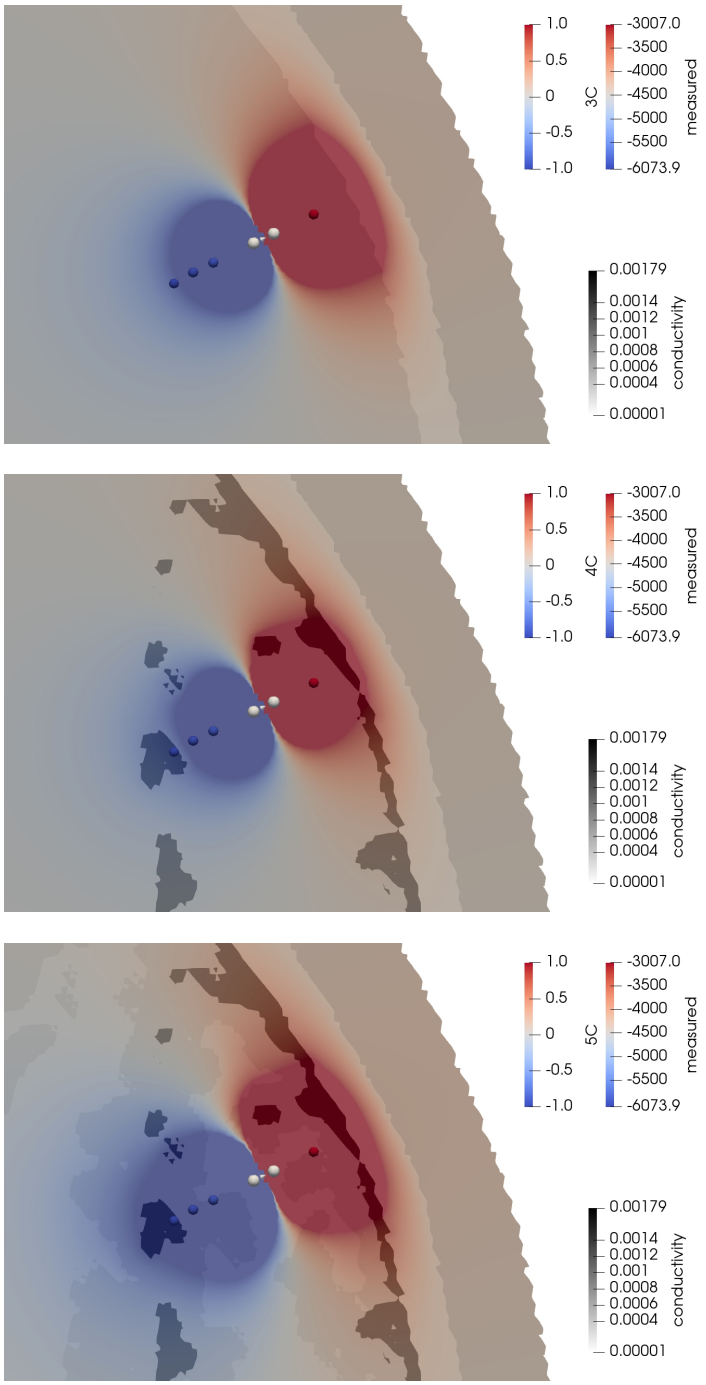

Figure 3.3 *Visualization of simulated potentials in 3C (top), 4C (center) and 5C (bottom) on a coronal plane of the volume conduction head model. Overlaid to the potentials are the conductivity profile values (gray values). The measured potential magnitude colors the 4 sphere visualized. The white sphere represents the anode and cathode.*

As a second study, we focused on the analysis of the RDM% and MAG% relative to each shaft, both for MP and BP.

First, we investigated the modulation of the mesh resolution on the errors. Therefore we fixed the source model to PI and we compared the results given from 1 mm and 2 mm. See Figure 3.4.

From Figure 3.4, top, we notice that 10 out of 14 shafts have an RDM% approximately below 10%. No strong modulation is given by the choice of the volume conduction head model. Moreover, results relative to the 2 mm mesh resolution are less accurate than the ones relative to the 1 mm mesh resolution only for those shafts whose RDM% is higher than 10%. From Figure 3.4, bottom, we observe high MAG% errors and we clearly see that results for 3C and 4C are better if compared to the ones of 5C.

Second, we analyzed the influence given by the choice of the source model: PI, SA and VEN. Since the modulation given by the mesh resolution was negligible, we focused on the results for 1 mm mesh resolution. See Figure 3.5.

From Figure 3.5, we can conclude that the choice of the source model, i.e., PI, SA and VEN, do not influence the error measures.

Finally, in Figure 3.6, we report the results for the BP data.

Overall, the RDM% and MAG% are higher than the one when MP is adopted. The same consideration for MP can be done for BP.

In conclusion, we fixed the source model to PI and the mesh resolution to 1 mm in the following analysis.

3.5.2 Global Comparison Results

In this subsection, we show global comparison results where we analyzed all the contacts, independently from the shafts where they are lying. Since we noticed from the previous subsection 3.5.1 that there is only a mild modulation on the relative error given by both the source model and the mesh resolution, in this subsection we fixed the mesh resolution to 1 mm and the source model to PI.

In Figure 3.7 the measured and simulated potentials are visualized, for both referencing systems, i.e., MP and BP, and for all the three head models, i.e., 3C, 4C and 5C. We additionally performed a paired t-test in order to evaluate the significance of the difference between measured and simulated potentials. In the case of MP, where the signal was re-referenced to the contact in white matter with the highest distance from the dipole position, the simulated potential relative to 3C (in blue) and 4C (in orange) are not significantly

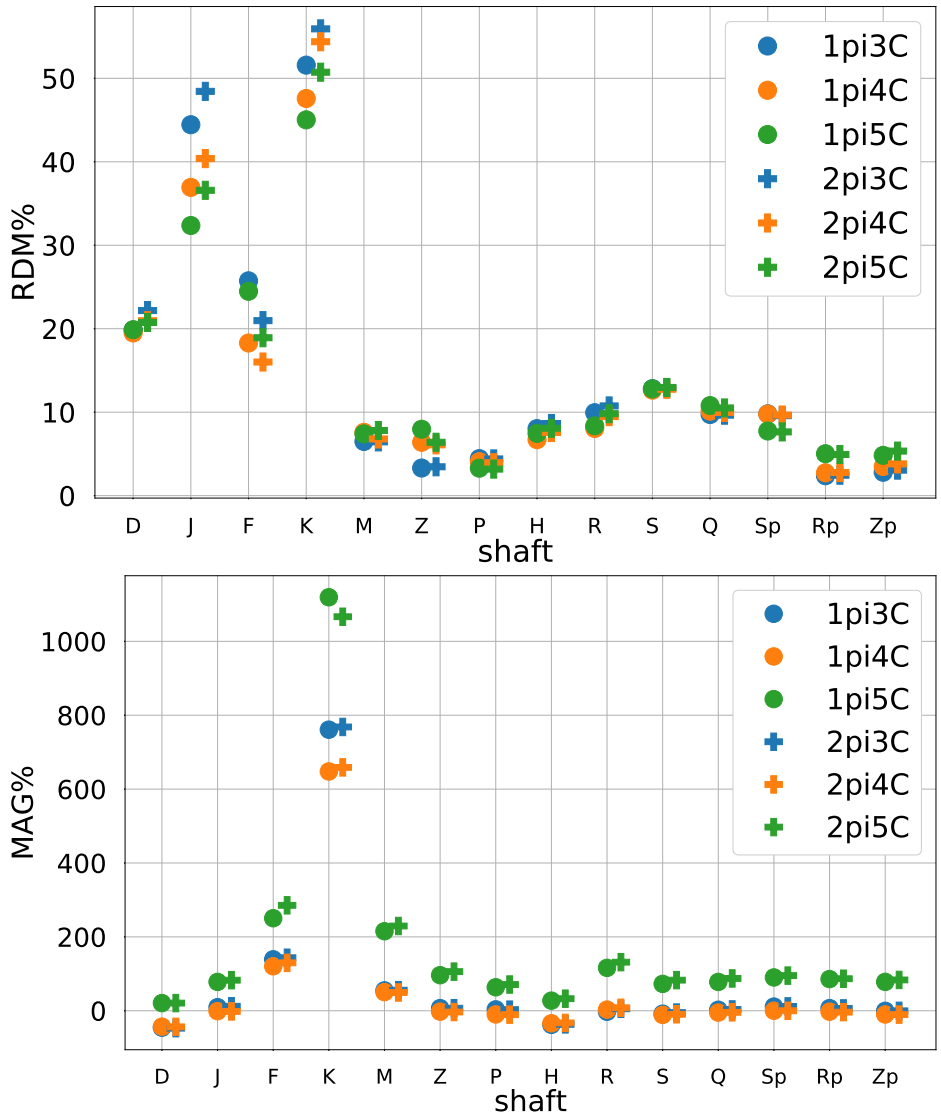

Figure 3.4 *RDM% comparison between 1 mm and 2 mm results relative to 3C (in blue), 4C (in orange) and 5C (in green) when the PI is adopted. The measured data are referenced to MP. On the x-axis are the shaft labels.*

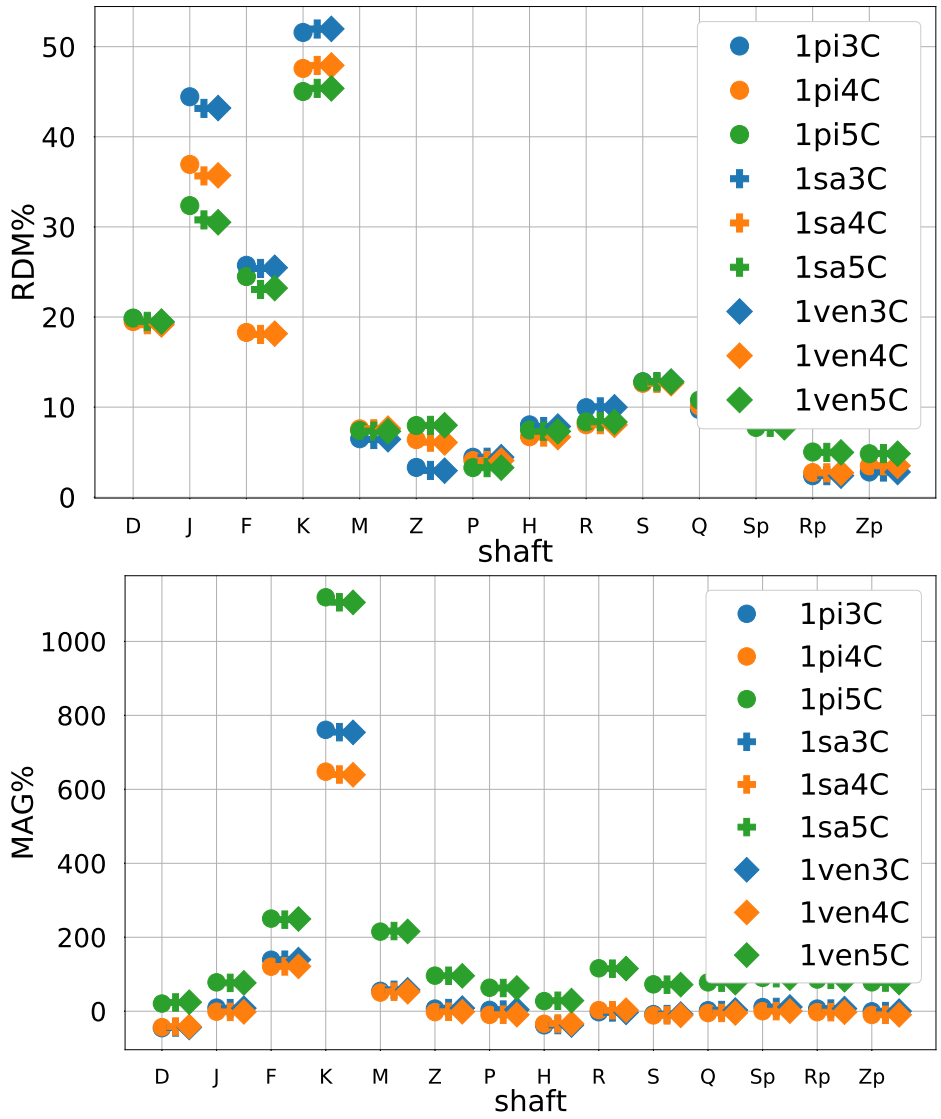

Figure 3.5 *RDM% and MAG% comparison between PI, SA, VEN results relative to 3C (in blue), 4C (in orange) and 5C (in green) when the 1 mm mesh is adopted. The measured data are referenced to MP. On the x-axis are the shaft labels.*

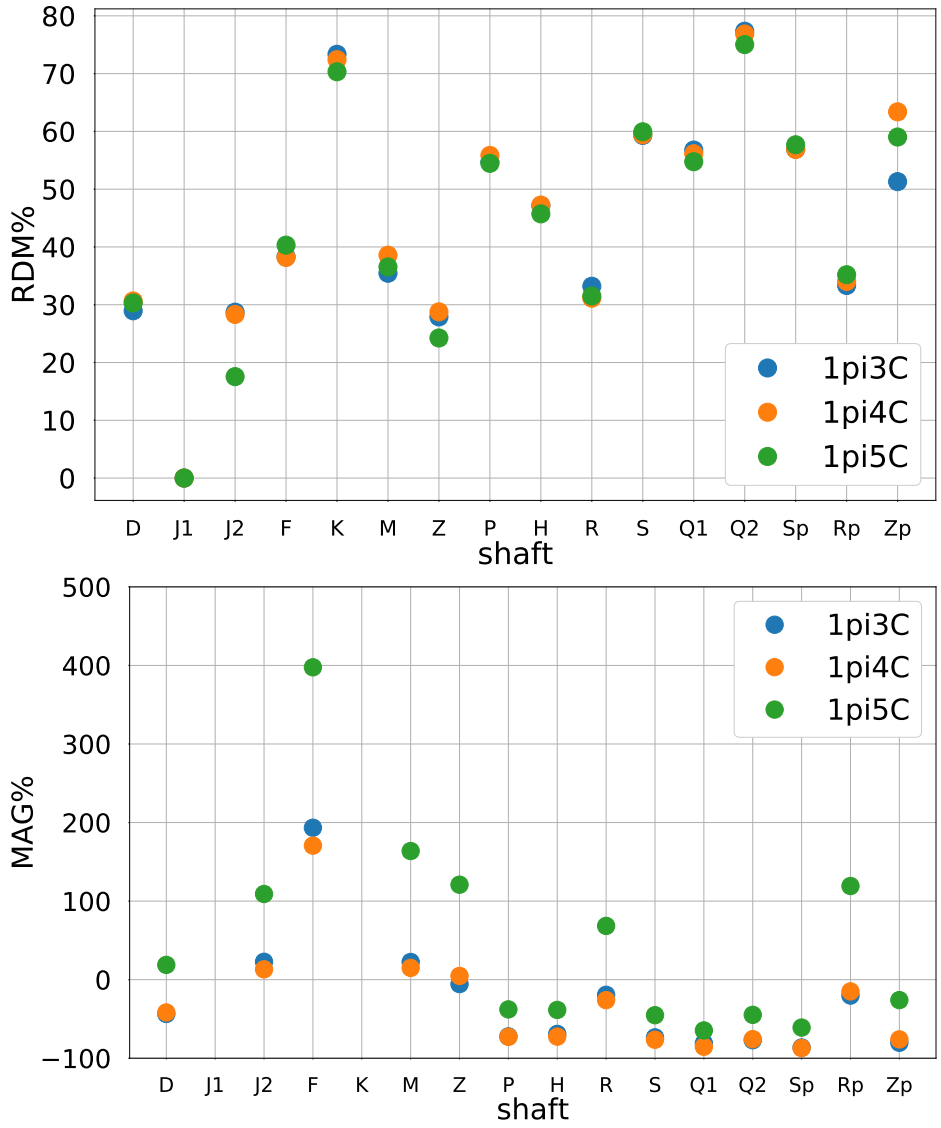

Figure 3.6 *RDM% comparison PI, SA, VEN results relative to 3C (in blue), 4C (in orange) and 5C (in green) when the 1 mm mesh is adopted. The measured data are referenced to BP. On the x-axis are the shaft labels.*

different from each other neither to the measured potential. In contrast, the simulated potential relative to 5C (in green) is significantly different from 3C, 4C and the measured potential, with the p-values of 10^{-11}, 10^{-14}, and 0.004, respectively. In the case of BP, where the signal was re-referenced between contiguous contacts within the same shaft, none of the differences are significant.

In Figure 3.8, we show the relative error in percentage between the measured potential with MP and BP referencing systems and the three simulation results, i.e., one for each head model (3C,4C,5C).

The results of the comparison in Figure 3.8 exhibit overall high relative errors, only 15% of the contacts has a RE% below 5%. A paired t-test reveals significant differences between 3C-5C and 4C-5C, with p-values of 10^{-5} and 0.003, respectively.

As a further analysis, we investigated whether the distance contact-dipole or the compartment of the contact modulate the relative errors.

In Figure 3.9, the histograms relative to the distance contact-dipole and to the compartment of the contact are visualized.

From the compartment histogram, Figure 3.9 at the bottom, we can notice that most of the contacts are in the white matter, and almost none are in the CSF compartment.

In Figure 3.10, we visualized the examined modulation of the distance contact-dipole through heatmaps.

From Figure 3.10, we see that the general behavior of the simulated data and the measured data are similar, but there is a crucial scaling difference.

Based on the histograms of Figure 3.9, we re-order and grouped the contacts accordingly. We therefore visualized in Figure 3.11 both the measured and simulated signals, when the contact order is given by the distance contact-dipole, on the x-axes.

As expected, the amplitude of the signals is are decreasing when the distance from the dipole is increasing, except for the last bin, where the trend is broken and the signals increase again. From Figure 3.11, we again notice a remarkable difference between the 5C simulated potential and all the other signals.

Moreover, in Figure 3.12, we can see the relative error in percentage between measured data (MP reference) and simulated data as a function of the distance contact-dipole.

From Figure 3.12, we clearly see a distance modulation of the relative error. For contacts closer to the dipole position, the relative error reaches its maximum value and it decreased when the distance is increasing. For the farthest contacts the relative error increases again, as it does the amplitude of the signal in Figure 3.11.

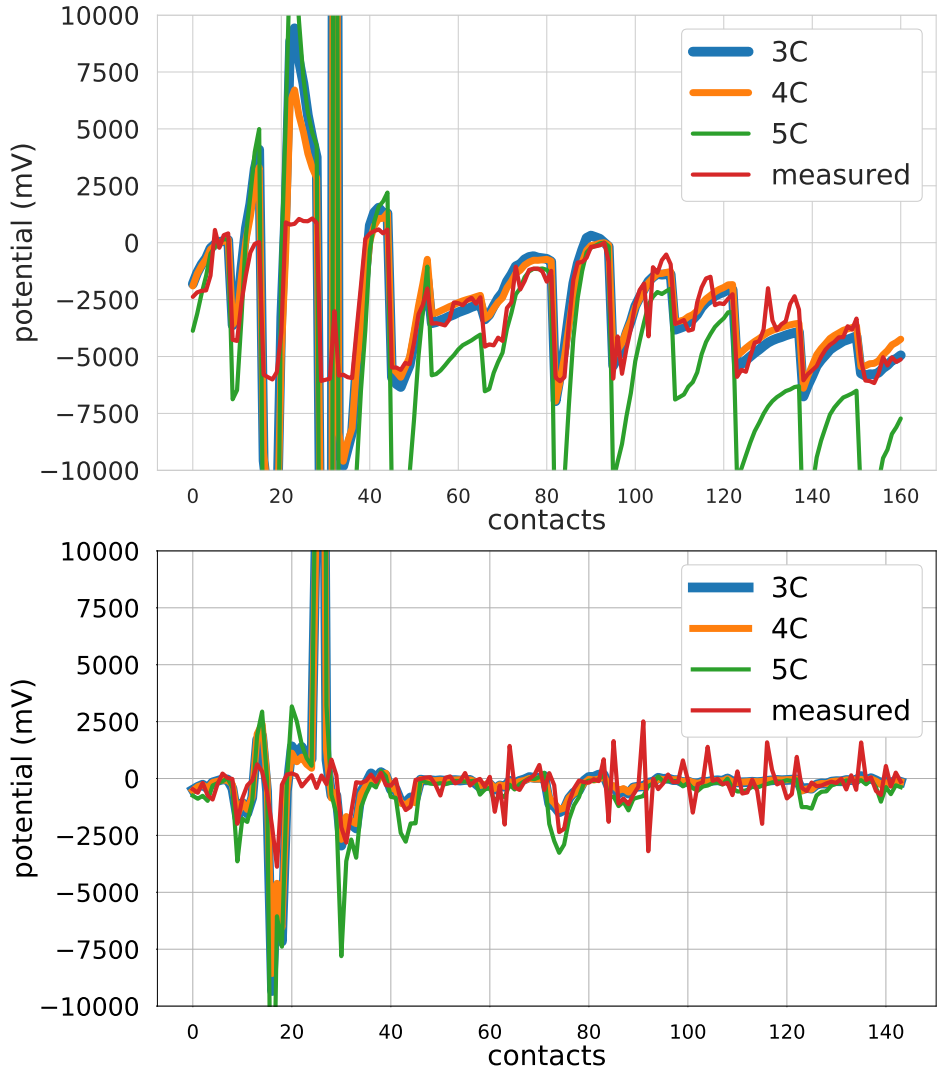

Figure 3.7 *Measured (in red) and simulated potentials. Top, the signal is re-referenced with the MP system; bottom, the signal is re-referenced with the BP system. The simulated potentials are relative to 3C, in blue, 4C, in orange, and to 5C, in green. On the x-axis, the contacts are ordered by label number.*

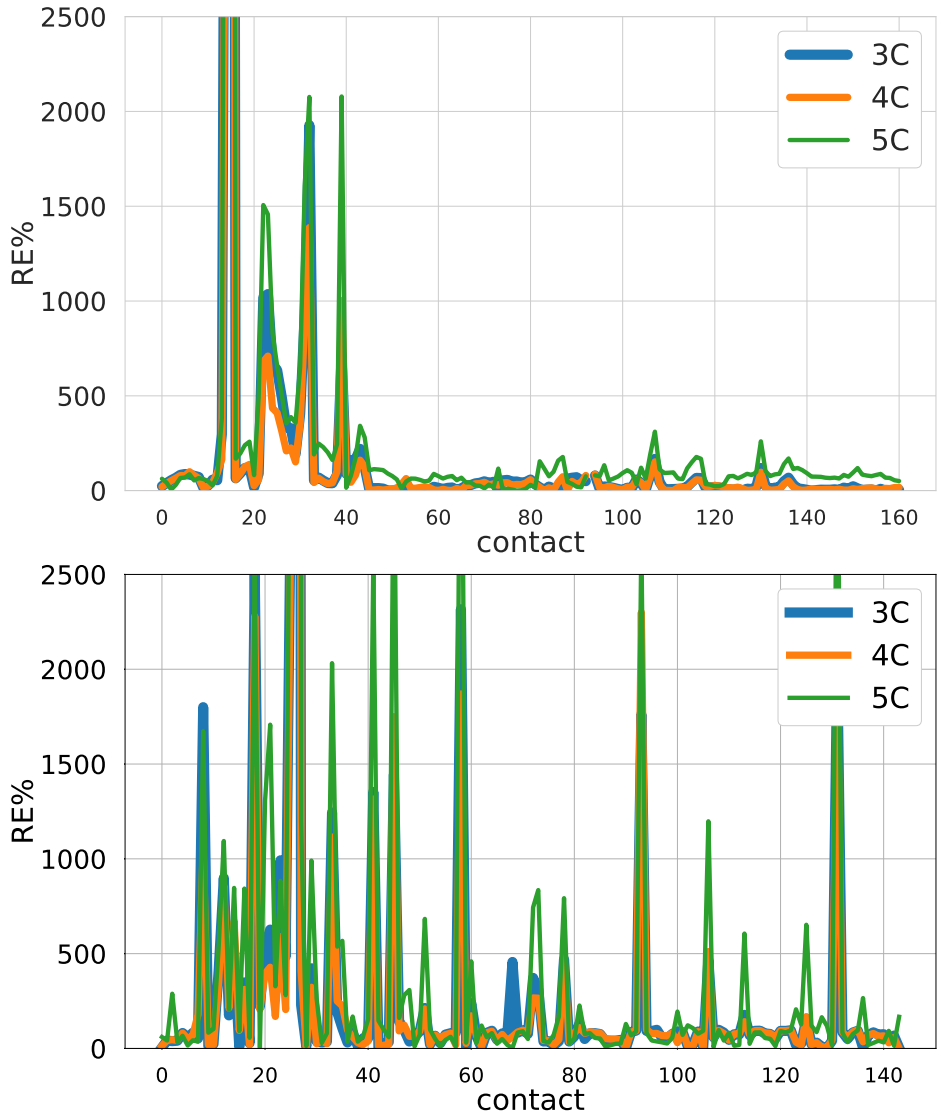

Figure 3.8 *Relative error in percentage between the measured data (in red) and simulated data (in blue for 3C, in orange for 4C, in green for 5C), when the MP (right) and the BP (left) referencing systems have been adopted. On the x-axis, the contacts are ordered by label number.*

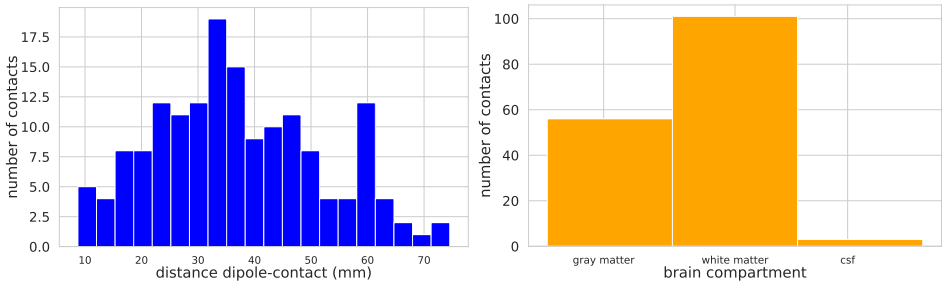

Figure 3.9 *Histograms of the distance contact-dipole, on the left, and of the compartment of the contact, on the right. The data we analyzed is relative to contacts which are only in the brain compartments: white matter, gray matter and CSF.*

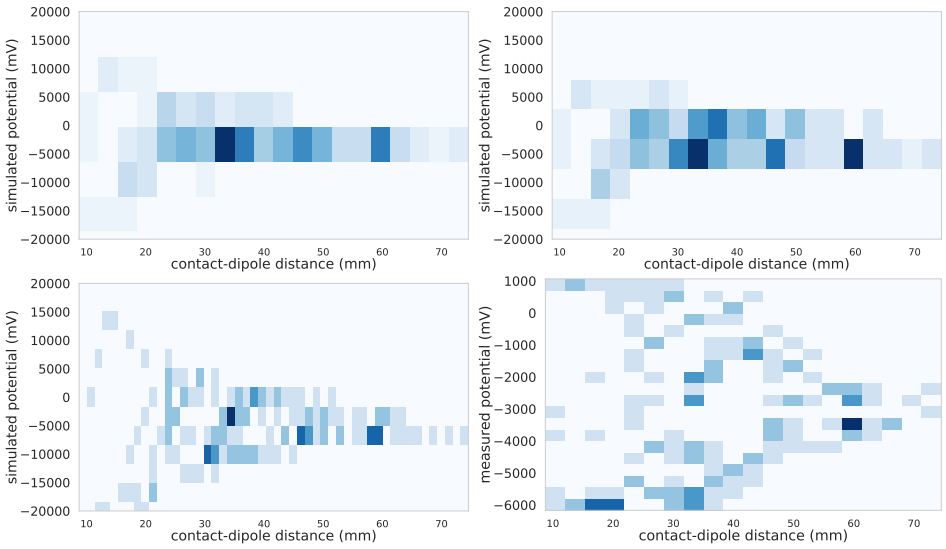

Figure 3.10 *Heatmaps distance contact-dipole for the simulated potential relative to 3C (upper row, left), to 4C (upper row, right), to 5C (lower row, left) and for the measured data (lower row, right). Note the different scaling of the z-axis.*

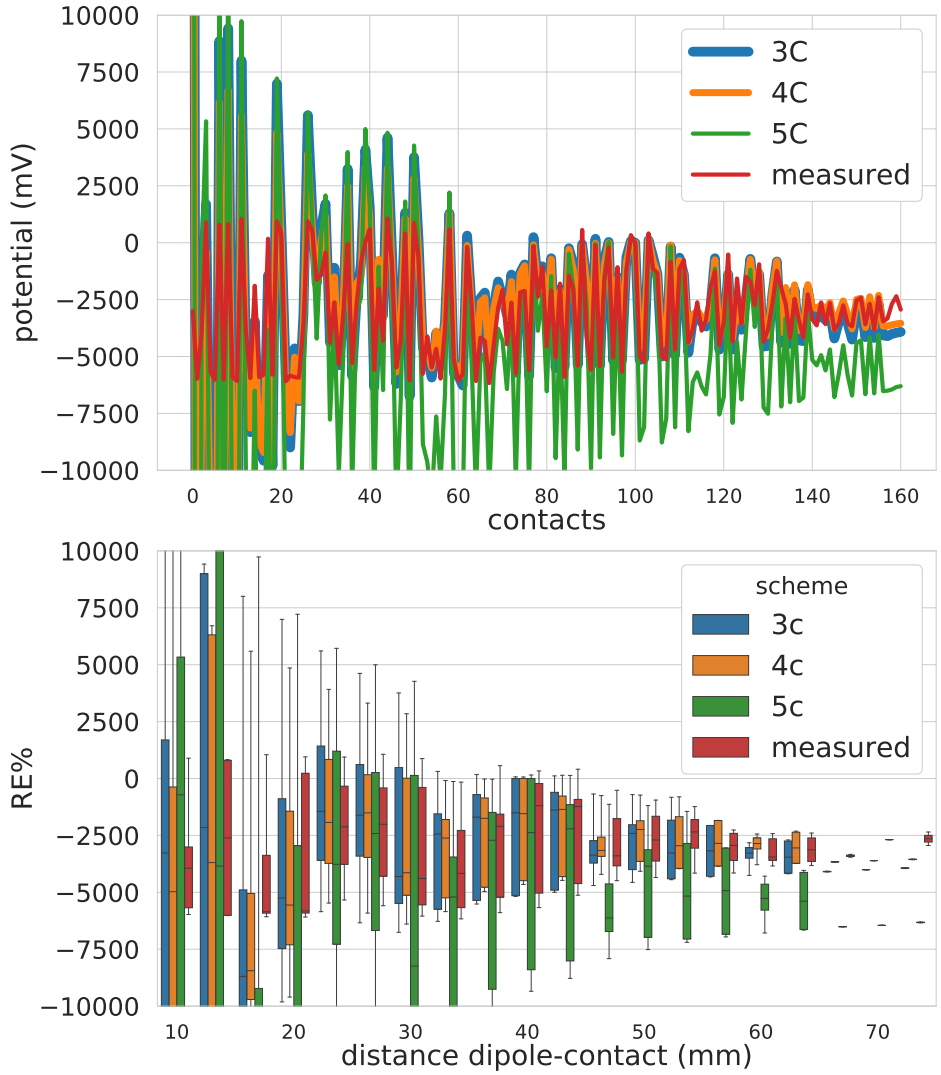

Figure 3.11 *Measured (in red) and simulated potentials. The simulated potentials are relative to 3C, in blue, 4C, in orange, and to 5C, in green. On the x-axis, the contacts are ordered by distance contact-dipole. Top, the signals are grouped following the histogram relative to the distances contact-dipole in Figure 3.9, bottom.*

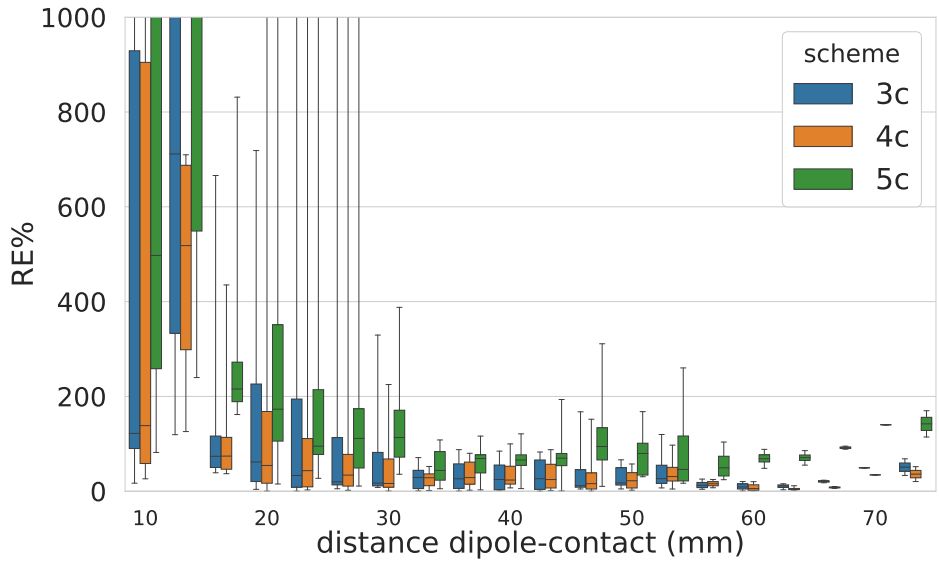

Figure 3.12 *Boxplot of the relative error between measure data (in MP reference) and the simulated data relative to 3C (in blue), 4C (in orange) and 5C (in green). Histograms of the distance contact-dipole, top, and of the compartment of the contact, bottom. The data we analyzed is relative to contacts which are only in the brain compartments: white matter, gray matter and CSF.*

Finally, we grouped the relative errors and contacts with respect to the compartment where the contacts are lying. Results are shown in Figure 3.12.

From Figure 3.13, we again notice that the simulation results relative to 5C are different from the simulation results relative to 3C and 4C, whose difference is negligible. In particular, the median RE% of the simulated potentials for the white matter grows from $\approx 19\%$ to $\approx 21\%$ and $\approx 75\%$ for 3C, 4C and 5C, respectively. In the gray matter compartment, the median RE% varies from $\approx 50\%$ to $\approx 34\%$ and $\approx 90\%$ for 3C, 4C and 5C, respectively. In the CSF compartment, the median RE% varies from $\approx 65\%$ to $\approx 60\%$ and more than $\approx 175\%$ for 3C, 4C and 5C, respectively.

3.6 Tools Used in the Pipeline

In the pipeline we used several tools:

- The pre-processing and creation of the volumetric masks was entirely performed via routines available in Fieldtrip (Oostenveld et al., 2011), in particular, the scalp and skull segmentation was done via the *spm12* software (Penny et al., 2011), embedded in Fieldtrip, see, for example, (Vorwerk et al., 2018).

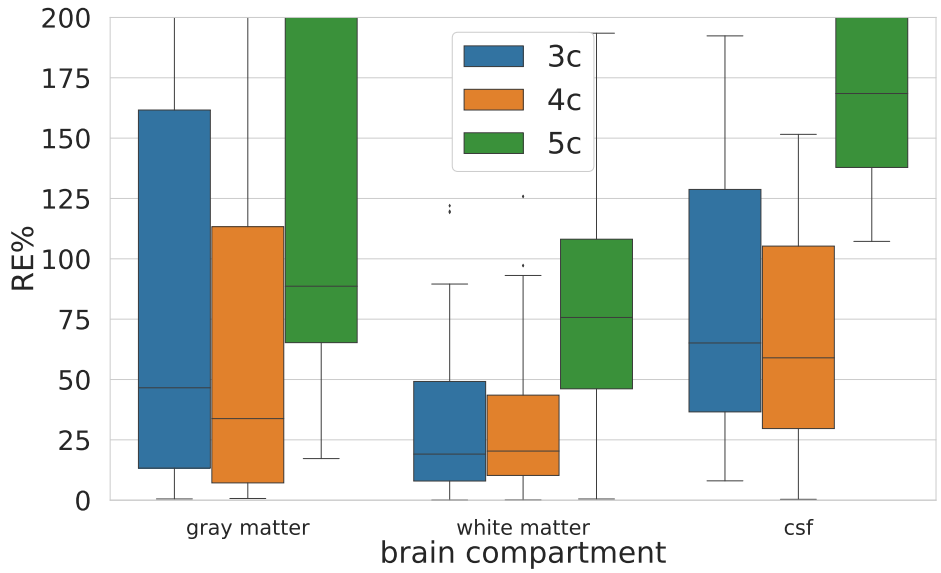

Figure 3.13 *Boxplot of the relative error between measure data (in MP reference) and the simulated data relative to 3C (in blue), 4C (in orange) and 5C (in green). On the x-axis, the contacts are grouped following the compartment where the contacts lie. The data we analyzed is relative to contacts which are only in the brain compartments: white matter, gray matter and CSF.*

- The Seg3d (CIBC, 2016) software was utilized for an easier visualization of both sliced volumetric masks and automatically generated surfaces, for checking the output of the segmentation and for performing the manual correction of the segmentation results.
- Fieldtrip and Matlab were adopted to process the sEEG electrophysiological signals.
- The forward simulation was conducted in the duneuro software, via the Python interface, and Paraview (Henderson et al., 2004) was used to visualized the simulated potentials and currents.

Chapter 4

Conclusions and Outlook

4.0.1 Conclusions

After a clinical, biological, mathematical and technological backgrounds in Chapter 1, we introduced the volume conduction and sEEG data in Chapter 2. In Chapter 2, we presented the theory related to the standard Lagrangian continuous Galerkin (CG-) and a discontinuous Galerkin (DG-) finite element methods (FEMs) to solve the (s)EEG forward problem. In Chapter 3 we conducted a comparison between simulated and measured potentials from one sEEG recording of electric stimulation. First, we simulated the potential generated by a dipole positioned between the actual anode and cathode. The simulations consist in solving the sEEG forward problem by means of a CG-FEM scheme implemented in the software *duneuro* (Nüßing et al., 2019). We computed the electric potential in three different volume conduction head models built from anatomical data, i.e., T1w MRI, where we considered different conductivity profiles, namely, a three compartment head model (3C) where the scalp, skull and brain compartments are considered; a four compartment head model (4C) where additionally to 3C the CSF compartment was identified; and a five compartment head model (5C) where the distinction between gray and white matter is modeled. Furthermore, we considered three different source models (PI, SA and VEN) and two different mesh resolution (1 mm and 2 mm). Second, we processed the sEEG dataset. We re-referenced the signal following two of the most used approaches, namely, a monopolar reference (MP), with the farther contact taken in the white compartment, and a bipolar reference (BP). We then applied a baseline correction, and we extracted the mean peak for each contact. Third, we compared the measured and simulated potentials. We divided the comparison into two main parts. In the first part we analyzed the differences between simulated and measured potentials within each of the shaft. In the second part we compared the simulated and measured signals

globally, i.e., independently from the shaft to which they belong. From the analysis in Chapter 3 we can conclude that:

- the CG-FEM method and code implemented in *duneuro* (Nüßing et al., 2019), which has been intensively tested in (Engwer et al., 2017; Nüßing et al., 2016) for scalp EEG (and in (Piastra et al., 2018) for MEG) is stable for sEEG when changing source model (PI, SA, VEN) and mesh resolution (1 mm and 2 mm), while the DG-FEM, in a first analysis, did not delivered reasonable results and therefore more investigations are needed;
- we were able to identify the responses of the brain stimulation in the actual measurements, in both configurations (MP and BP);
- when analyzing the single shaft behavior, we could see a match in the pattern within a neighborhood of the anode-cathode, but the scaling was not consistent;
- the choice of mesh resolution and source model did not influence the topographical (RDM%) and magnitude (MAG%) error;
- from the MAG% results we conclude that, within this framework, 4C and 3C delivered more accurate results if compared to the ones for 5C, both in the MP and BP configurations;
- as to the global comparison analysis, we conclude that there are both a distance contact-dipole and a compartment modulation of the relative error, which are overall very high. In particular, for contacts in the white matter, we observed the most accurate results;
- also in the case of the global comparison, results for 3C and 4C were more accurate than the ones for 5C.

This work aims at investigating the approach which can lead to a validation of the volume conduction head model with electric brain stimulations via sEEG and it represents a first attempt into this direction. The thesis is therefore focused on the methods and tools needed to build a ground truth of a volume conduction model from measured data, which can be used in a validation of the model, when the data of more patients are considered.

Many studies have been conducted in order to quantify the sensitivity of the numerical methods and VC simulation solutions to, for example, the head model, the sensor model, the source model. In (Vorwerk et al., 2014), a guideline for EEG and MEG forward modeling using FEM was presented in realistic head models with a varying number of layers and

conductivity profiles. The main result was that it is highly recommended to include the cerebrospinal fluid (CSF) compartment and distinguish between gray and white matter. Furthermore, especially for the MEG, the modeling of skull spongiosa and compacta might be neglected. The numerical errors of a lower resolved (about 1 million nodes) 6 compartment anisotropic (6CA) model in reference to a higher resolved (about 2 million nodes) version of 6CA were analyzed and expressed in terms of topography and magnitude errors: 95% of the sources had a topographical error of less than 2.5% and a magnitude error of less than 10%. Recently, a discontinuous Galerkin FEM (DG-FEM) EEG forward approach has been proposed as an alternative to a standard lagrangian FEM (Engwer et al., 2017). It was shown that DG-FEM preserves the property of conservation of charge and that it can, in certain situations such as the so-called skull leakages, be superior to the standard FEM approach. The same method was applied for solving the MEG forward problem (Piastra et al., 2018). While in the EEG case, in presence of skull leakages, DG-FEM outperformed the standard FEM, in MEG, DG-FEM achieved similar numerical errors as the standard FEM approach, i.e., skull leakages do not play a role for the MEG modality. However, if the goal is a combined source analysis of EEG and MEG data, it is highly desirable to employ the same forward model for both EEG and MEG data. Therefore, the newly presented conservative DG-FEM can at least complement and in some scenarios even outperform the established standard FEM approaches in EEG or combined MEG/EEG source analysis scenarios, which motivates a further evaluation of DG-FEM for applications in bioelectromagnetism. Other FEMs have been implemented and analyzed, e.g., (Nüßing et al., 2016; Vorwerk et al., 2017). Nevertheless, to the best of our knowledge, in none of these studies VC simulation results were compared with actual measurements, i.e., a ground truth.

Validations with measured dataset have been conducted.

In (Gullmar et al., 2006), for example, they investigated the influence of anisotropic conductivity on EEG source reconstruction with actual and simulated potentials in rabbits.

In (Leahy et al., 1998), they conducted a study about the dipole localization accuracy for MEG and EEG using a human skull phantom.

In both these examples, the validation was conducted by comparing source localization results, which is not what we aimed at in this work.

Finally, in (Murakami et al., 2016) and in (Dalal et al., 2013), they investigated the correlation between MEG to sEEG in patients undergoing epilepsy surgery and the ability of MEG to capture oscillatory modulations in the neocortex and the hippocampus via a simultaneous MEG-sEEG dataset, respectively.

4.1 Outlook

We now discuss possibilities for further accuracy increase that we plan to evaluate in our future work:

- in this study the volume conduction head model was taken isotropic, therefore a possible improvement can be obtained when taking into account the anisotropy of the white matter, whenever the DTI data of the patient is available;
- the DG-FEM approach represents an interesting alternative to the standard CG-FEM, which might improve the accuracy of the simulation results, as its focus is on the conservation of charge property;
- in this work, only a baseline correction of the signal was performed. More elaborated pre-processing steps might improve the correct interpretation of the data;
- only two referencing systems were analyzed in this work, i.e., MP and BP. Therefore, a more sophisticated re-referencing method such as the one described in (Arnulfo et al., 2015a) might improve the signal understanding;
- including more subjects and create a statistics out of topographical and magnitude errors will lead to the desired validation of volume conduction models and a more generalized guideline on how to build a volume conduction model can be then extrapolated.

References

Acar, Z. A. and Makeig, S. (2010). Neuroelectromagnetic forward head modeling toolbox. *Journal of neuroscience methods*, 190(2):258–270.

Almeida, A. N., Martinez, V., and Feindel, W. (2005). The first case of invasive eeg monitoring for the surgical treatment of epilepsy: historical significance and context. *Epilepsia*, 46(7):1082–1085.

Arnulfo, G., Hirvonen, J., Nobili, L., Palva, S., and Palva, J. M. (2015a). Phase and amplitude correlations in resting-state activity in human stereotactical eeg recordings. *Neuroimage*, 112:114–127.

Arnulfo, G., Narizzano, M., Cardinale, F., Fato, M. M., and Palva, J. M. (2015b). Automatic segmentation of deep intracerebral electrodes in computed tomography scans. *BMC bioinformatics*, 16(1):99.

Awada, K. A., Jackson, D. R., Williams, J. T., Wilton, D. R., Baumann, S. B., and Papanicolaou, A. C. (1997). Computational aspects of finite element modeling in EEG source localization. *IEEE Transactions on Biomedical Engineering*, 44(8):736–752.

Bailey, P. and Gibbs, F. A. (1951). The surgical treatment of psychomotor epilepsy. *Journal of the American Medical Association*, 145(6):365–370.

Barr de Saint-Venant, A. (1853). Memoire sur la torsion des prismes. *CR Acad. Sci*, 37.

Bastian, P. and Blatt, M. (2007). Iterative Solver Template Library.

Bastian, P., Blatt, M., Dedner, A., Engwer, C., Klöfkorn, R., Kornhuber, R., Ohlberger, M., and Sander, O. (2008a). A generic grid interface for parallel and adaptive scientific computing. part II: Implementation and tests in DUNE. *Computing*, 82(2-3):121–138.

Bastian, P., Blatt, M., Dedner, A., Engwer, C., Klöfkorn, R., Ohlberger, M., and Sander, O. (2008b). A generic grid interface for parallel and adaptive scientific computing. part I: abstract framework. *Computing*, 82(2):103–119.

Baumann, S. B., Wozny, D. R., Kelly, S. K., and Meno, F. M. (1997). The electrical conductivity of human cerebrospinal fluid at body temperature. *IEEE Transactions on Biomedical Engineering*, 44(3):220–223.

Berger, H. (1929). Über das elektrenkephalogramm des menschen. *European archives of psychiatry and clinical neuroscience*, 87(1):527–570.

Bertrand, O., Thevenet, M., and Perrin, F. (1991). 3D finite element method in brain electrical activity studies. *Biomagnetic Localization and 3D Modelling*, pages 154–171.

Brette, R. and Destexhe, A. (2012). *Handbook of neural activity measurement*. Cambridge University Press.

Buchner, H., Knoll, G., Fuchs, M., Rienäcker, A., Beckmann, R., Wagner, M., Silny, J., and Pesch, J. (1997). Inverse localization of electric dipole current sources in finite element models of the human head. *Electroencephalography and clinical Neurophysiology*, 102(4):267–278.

Cardinale, F., Cossu, M., Castana, L., Casaceli, G., Schiariti, M. P., Miserocchi, A., Fuschillo, D., Moscato, A., Caborni, C., Arnulfo, G., et al. (2012). Stereoelectroencephalography: surgical methodology, safety, and stereotactic application accuracy in 500 procedures. *Neurosurgery*, 72(3):353–366.

Ciarlet, P. G. (2002). The finite element method for elliptic problems. *Classics in applied mathematics*, 40:1–511.

CIBC (2016). Seg3D: Volumetric Image Segmentation and Visualization. Scientific Computing and Imaging Institute (SCI), Download from: http://www.seg3d.org.

Cohen, D. (1972). Magnetoencephalography: detection of the brain's electrical activity with a superconducting magnetometer. *Science*, 175(4022):664–666.

Cook, M. J. and Koles, Z. J. (2006). A high-resolution anisotropic finite-volume head model for EEG source analysis. In *Engineering in Medicine and Biology Society, 2006. EMBS'06. 28th Annual International Conference of the IEEE*, pages 4536–4539. IEEE.

Dalal, S., Jerbi, K., Bertrand, O., Adam, C., Ducorps, A., Schwartz, D., Martinerie, J., and Lachaux, J.-P. (2013). Simultaneous meg-intracranial eeg: new insights into the ability of meg to capture oscillatory modulations in the neocortex and the hippocampus. *Epilepsy and Behavior*, pages 10–1016.

Dannhauer, M., Lanfer, B., Wolters, C. H., and Knösche, T. R. (2011). Modeling of the human skull in EEG source analysis. *Human brain mapping*, 32(9):1383–1399.

David, O., Blauwblomme, T., Job, A.-S., Chabardès, S., Hoffmann, D., Minotti, L., and Kahane, P. (2011). Imaging the seizure onset zone with stereo-electroencephalography. *Brain*, 134(10):2898–2911.

de la Salud. Programme for Neurological Diseases, O. M., Organization, W. H., against Epilepsy, G. C., for Neurological Diseases, P., Organization), N. W. H., for Epilepsy, I. B., of Mental Health, W. H. O. D., Abuse, S., of Epilepsy, I. B., and against Epilepsy, I. L. (2005). *Atlas: Epilepsy Care in the World*. World Health Organization.

De Munck, J. C., Van Dijk, B. W., and Spekreijse, H. (1988). Mathematical dipoles are adequate to describe realistic generators of human brain activity. *IEEE Transactions on Biomedical Engineering*, 35(11):960–966.

Devinsky, O., Vezzani, A., O'Brien, T., Jette, N., E. Scheffer, I., de Curtis, M., and Perucca, P. (2018). Epilepsy. *Nature Reviews Disease Primers*, 4:18024.

Di Pietro, D. A., Ern, A., and Guermond, J.-L. (2008). Discontinuous galerkin methods for anisotropic semidefinite diffusion with advection. *SIAM Journal on Numerical Analysis*, 46(2):805–831.

Drechsler, F., Wolters, C. H., Dierkes, T., Si, H., and Grasedyck, L. (2009). A full subtraction approach for finite element method based source analysis using constrained Delaunay tetrahedralisation. *NeuroImage*, 46(4):1055–1065.

Engwer, C., Vorwerk, J., Ludewig, J., and Wolters, C. H. (2017). A discontinuous galerkin method to solve the eeg forward problem using the subtraction approach. *SIAM Journal on Scientific Computing*, 39(1):B138–B164.

Fisher, R. S., Acevedo, C., Arzimanoglou, A., Bogacz, A., Cross, J. H., Elger, C. E., Engel Jr, J., Forsgren, L., French, J. A., Glynn, M., et al. (2014). Ilae official report: a practical clinical definition of epilepsy. *Epilepsia*, 55(4):475–482.

Fisher, R. S., Cross, J. H., French, J. A., Higurashi, N., Hirsch, E., Jansen, F. E., Lagae, L., Moshé, S. L., Peltola, J., Roulet Perez, E., et al. (2017). Operational classification of seizure types by the international league against epilepsy: Position paper of the ilae commission for classification and terminology. *Epilepsia*, 58(4):522–530.

Giani, S. and Houston, P. (2011). Anisotropic hp-adaptive discontinuous galerkin finite element methods for compressible fluid flows. *International Journal of Numerical Analysis and Modeling*.

Gloor, P. (1969). Hans berger-on the electroencephalogram of man. *Electroenceph Clin Neurophysiol*.

Gnatkovsky, Vadym, M. D. C. C. P. F. C. G. L. R. R. M. L. N. I. S. L. T. and Francione, S. (2014). Biomarkers of epileptogenic zone defined by quantified stereo-eeg analysis. *Epilepsia*, 55(2):296–305.

Golgi, C. (1873). Sulla struttura della sostanza grigia del cervello. *Gazz. Med. Ital. Lomb.*, 33:244–246.

Gullmar, D., Haueisen, J., Eiselt, M., Gießler, F., Flemming, L., Anwander, A., Knosche, T. R., Wolters, C. H., Dumpelmann, M., Tuch, D. S., et al. (2006). Influence of anisotropic conductivity on eeg source reconstruction: investigations in a rabbit model. *IEEE Transactions on Biomedical Engineering*, 53(9):1841–1850.

Hallez, H., Vanrumste, B., Grech, R., Muscat, J., De Clercq, W., Vergult, A., D'Asseler, Y., Camilleri, K. P., Fabri, S. G., Van Huffel, S., et al. (2007). Review on solving the forward problem in eeg source analysis. *Journal of neuroengineering and rehabilitation*, 4(1):46.

Hämäläinen, M., Hari, R., Ilmoniemi, R. J., Knuutila, J., and Lounasmaa, O. V. (1993). Magnetoencephalography—theory, instrumentation, and applications to noninvasive studies of the working human brain. *Reviews of modern Physics*, 65(2):413.

Henderson, A., Ahrens, J., Law, C., et al. (2004). *The ParaView Guide*, volume 366. Kitware Clifton Park, NY.

Kahane, P., Landré, E., Minotti, L., Francione, S., and Ryvlin, P. (2006). The bancaud and talairach view on the epileptogenic zone: a working hypothesis. *Epileptic disorders*, 8(2):16–26.

Kovac, S., Kahane, P., and Diehl, B. (2016). Seizures induced by direct electrical cortical stimulation–mechanisms and clinical considerations. *Clinical Neurophysiology*, 127(1):31–39.

Kovac, S., Rodionov, R., Chinnasami, S., Wehner, T., Scott, C. A., McEvoy, A. W., Miserocchi, A., and Diehl, B. (2014a). Clinical significance of nonhabitual seizures during intracranial eeg monitoring. *Epilepsia*, 55(1):e1–e5.

Kovac, S., Scott, C. A., Maglajlija, V., Rodionov, R., McEvoy, A. W., and Diehl, B. (2011). Extraoperative electrical cortical stimulation: characteristics of motor responses and correlation with precentral gyrus. *Journal of Clinical Neurophysiology*, 28(6):618–624.

Kovac, S., Scott, C. A., Maglajlija, V., Toms, N., Rodionov, R., Miserocchi, A., McEvoy, A. W., and Diehl, B. (2014b). Comparison of bipolar versus monopolar extraoperative electrical cortical stimulation mapping in patients with focal epilepsy. *Clinical Neurophysiology*, 125(4):667–674.

Kovac, S., Vakharia, V. N., Scott, C., and Diehl, B. (2017). Invasive epilepsy surgery evaluation. *Seizure*, 44:125–136.

Kuzniecky, R. I. and Jackson, G. D. (1995). *Magnetic resonance in epilepsy*. Lippincott Williams & Wilkins.

Leahy, R., Mosher, J., Spencer, M., Huang, M., and Lewine, J. (1998). A study of dipole localization accuracy for meg and eeg using a human skull phantom. *Electroencephalography and clinical neurophysiology*, 107(2):159–173.

Macewen, W. (1879). Tumour of the dura mater removed during life in a person affected with epilepsy. *Glas Med J*, 12:210.

Mantoan Ritter, L., Golshani, P., Takahashi, K., Dufour, S., Valiante, T., and Kokaia, M. (2014). Wonoep appraisal: optogenetic tools to suppress seizures and explore the mechanisms of epileptogenesis. *Epilepsia*, 55(11):1693–1702.

Marin, G., Guerin, C., Baillet, S., Garnero, L., and Meunier, G. (1998). Influence of skull anisotropy for the forward and inverse problem in EEG: simulation studies using FEM on realistic head models. *Human brain mapping*, 6(4):250–269.

Medani, T., Lautru, D., Schwartz, D., Ren, Z., and Sou, G. (2015). Fem method for the eeg forward problem and improvement based on modification of the saint venant's method. *Progress In Electromagnetics Research*, 153:11–22.

Montes-Restrepo, V., van Mierlo, P., Strobbe, G., Staelens, S., Vandenberghe, S., and Hallez, H. (2014). Influence of skull modeling approaches on EEG source localization. *Brain topography*, 27(1):95–111.

Mosher, J. C., Leahy, R. M., and Lewis, P. S. (1999). EEG and MEG: forward solutions for inverse methods. *IEEE Transactions on Biomedical Engineering*, 46(3):245–259.

Mullin, J. P., Shriver, M., Alomar, S., Najm, I., Bulacio, J., Chauvel, P., and Gonzalez-Martinez, J. (2016). Is seeg safe? a systematic review and meta-analysis of stereo-electroencephalography–related complications. *Epilepsia*, 57(3):386–401.

Murakami, H., Wang, Z. I., Marashly, A., Krishnan, B., Prayson, R. A., Kakisaka, Y., Mosher, J. C., Bulacio, J., Gonzalez-Martinez, J. A., Bingaman, W. E., et al. (2016). Correlating magnetoencephalography to stereo-electroencephalography in patients undergoing epilepsy surgery. *Brain*, 139(11):2935–2947.

Murakami, S. and Okada, Y. (2006). Contributions of principal neocortical neurons to magnetoencephalography and electroencephalography signals. *The Journal of physiology*, 575(3):925–936.

Narizzano, M., Arnulfo, G., Ricci, S., Toselli, B., Tisdall, M., Canessa, A., Fato, M. M., and Cardinale, F. (2017). Seeg assistant: a 3dslicer extension to support epilepsy surgery. *BMC bioinformatics*, 18(1):124.

Nitsche, J. (1971). Über ein variationsprinzip zur lösung von dirichlet-problemen bei verwendung von teilräumen, die keinen randbedingungen unterworfen sind. In *Abhandlungen aus dem mathematischen Seminar der Universität Hamburg*, volume 36, pages 9–15. Springer.

Nüßing, A., Piastra, M. C., Schrader, S., Miinalainen, T., Brinck, H., Wolters, C. H., and Engwer, C. (2019). duneuro - a software toolbox for forward modeling in neuroscience. *http://arxiv.org/abs/1901.02874*.

Nüßing, A., Wolters, C. H., Brinck, H., and Engwer, C. (2016). The unfitted discontinuous Galerkin method for solving the EEG forward problem. *IEEE Transactions on Biomedical Engineering*, 63(12):2564–2575.

Okada, Y. (1993). Empirical bases for constraints in current-imaging algorithms. *Brain topography*, 5(4):373–377.

Oostenveld, R., Fries, P., Maris, E., and Schoffelen, J.-M. (2011). Fieldtrip: open source software for advanced analysis of meg, eeg, and invasive electrophysiological data. *Computational intelligence and neuroscience*, 2011:1.

Penny, W. D., Friston, K. J., Ashburner, J. T., Kiebel, S. J., and Nichols, T. E. (2011). *Statistical parametric mapping: the analysis of functional brain images*. Elsevier.

Piastra, M. C., Nüßing, A., Vorwerk, J., Bornfleth, H., Oostenveld, R., Engwer, C., and Wolters, C. H. (2018). The discontinuous galerkin finite element method for solving the meg and the combined meg/eeg forward problem. *Frontiers in Neuroscience*, 12:30.

Pursiainen, S., Vorwerk, J., and Wolters, C. H. (2016). Electroencephalography (EEG) forward modeling via H (div) finite element sources with focal interpolation. *Physics in medicine and biology*, 61(24):8502.

Purves, D., Augustine, G. J., Fitzpatrick, D., Hall, W. C., LaMantia, A.-S., Mooney, R. D., Platt, M. L., and White, L. E., editors (2018). *Neuroscience*. Springer, 6th edition.

Quarteroni, A. and Quarteroni, S. (2009). *Numerical models for differential problems*, volume 2. Springer.

Ramon, C., Schimpf, P., Haueisen, J., Holmes, M., and Ishimaru, A. (2004). Role of soft bone, CSF and gray matter in EEG simulations. *Brain topography*, 16(4):245–248.

Reynolds, E. H. and Trimble, M. R. (2009). Epilepsy, psychiatry, and neurology. *Epilepsia*, 50:50–55.

Rosenow, F. and Lüders, H. (2001). Presurgical evaluation of epilepsy. *Brain*, 124(9):1683–1700.

Schimpf, P. H., Ramon, C., and Haueisen, J. (2002). Dipole models for the EEG and MEG. *Biomedical Engineering, IEEE Transactions on*, 49(5):409–418.

Stenroos, M. and Sarvas, J. (2012). Bioelectromagnetic forward problem: isolated source approach revis (it) ed. *Physics in medicine and biology*, 57(11):3517.

Talairach, J., Bancaud, J., Bonis, A., Szikla, G., and Tournoux, P. (1962). Functional stereotaxic exploration of epilepsy. *Stereotactic and Functional Neurosurgery*, 22(3-5):328–331.

Todd, R. B. (1849). On the pathology and treatment of convulsive diseases. *Lond Med Gaz*, 8:661–671.

Vatta, F., Meneghini, F., Esposito, F., Mininel, S., and Di Salle, F. (2009). Solving the forward problem in EEG source analysis by spherical and fdm head modeling: a comparative analysis-biomed 2009. *Biomedical sciences instrumentation*, 45:382–388.

von Ellenrieder, N., Beltrachini, L., and Muravchik, C. H. (2012). Electrode and brain modeling in stereo-eeg. *Clinical Neurophysiology*, 123(9):1745–1754.

Vorwerk, J. (2016). *New finite element methods to solve the EEG/MEG forward problem*. PhD thesis, PhD thesis in Mathematics, Westfälische Wilhelms-Universität Münster.

Vorwerk, J., Cho, J.-H., Rampp, S., Hamer, H., Knösche, T. R., and Wolters, C. H. (2014). A guideline for head volume conductor modeling in EEG and MEG. *NeuroImage*, 100:590–607.

Vorwerk, J., Engwer, C., Pursiainen, S., and Wolters, C. H. (2017). A mixed finite element method to solve the eeg forward problem. *IEEE transactions on medical imaging*, 36(4):930–941.

Vorwerk, J., Oostenveld, R., Piastra, M. C., Magyari, L., and Wolters, C. H. (2018). The fieldtrip-simbio pipeline for eeg forward solutions. *Biomedical engineering online*, 17(1):37.

Wendel, K., Narra, N. G., Hannula, M., Kauppinen, P., and Malmivuo, J. (2008). The influence of CSF on EEG sensitivity distributions of multilayered head models. *IEEE Transactions on Biomedical Engineering*, 55(4):1454–1456.

Wiebe, S., Blume, W. T., Girvin, J. P., and Eliasziw, M. (2001). A randomized, controlled trial of surgery for temporal-lobe epilepsy. *New England Journal of Medicine*, 345(5):311–318.

Wolters, C. H., Köstler, H., Möller, C., Härdtlein, J., and Anwander, A. (2007). Numerical approaches for dipole modeling in finite element method based source analysis. In *International Congress Series*, volume 1300, pages 189–192. Elsevier.

Zimmerman, J., Thiene, P., and Harding, J. (1970). Design and operation of stable rf-biased superconducting point-contact quantum devices, and a note on the properties of perfectly clean metal contacts. *Journal of Applied Physics*, 41(4):1572–1580.